The Permeability Evolution of Tuffisites and Implications for Outgassing Through Dense Rhyolitic Magma

Michael Heap, Hugh Tuffen, Fabian Wadsworth, Thierry Reuschlé, Jonathan Castro, C. Ian Schipper

The permeability evolution of tuffisites and implications for outgassing through dense rhyolitic magma

Michael J. Heap[1]*, Hugh Tuffen[2], Fabian B. Wadsworth[3], Thierry Reuschlé[1], Jonathan M. Castro[4], and C. Ian Schipper[5]

[1]*Institut de Physique de Globe de Strasbourg, Université de Strasbourg, École et Observatoire des Sciences de la Terre (UMR 7516 CNRS), 5 rue René Descartes, 67084 Strasbourg, France*

[2]*Lancaster Environment Centre, Lancaster University, Lancaster LA1 4YQ, UK*

[3]*Department of Earth Sciences, Durham University, Durham, UK*

[4]*Institute of Geosciences, Johannes Gutenberg University Mainz, J.-J.-Becher-Weg 21, D-55128 Mainz, Germany*

[5]*School of Geography, Environment and Earth Sciences, Victoria University of Wellington, Kelburn Parade, Wellington 6012, New Zealand*

Corresponding author: M.J. Heap (heap@unistra.fr)

ORCID ID of corresponding author: https://orcid.org/0000-0002-4748-735X

Key points:

1. Permeability of variably sintered tuffisites from Chaitén and Cordón Caulle is between 10^{-16} and 10^{-15} m^2.
2. Surface tension and compaction-driven sintering timescales are between 2 min and 13.6 h and between 3.5 s and 5 min, respectively.

3. Inferred timescales of sintering-driven tuffisite compaction coincide with observed vent pulsations during hybrid rhyolitic activity

Abstract

There is growing evidence that outgassing through transient fracture networks exerts an important control on conduit processes and explosive-effusive activity during silicic eruptions. Indeed, the first modern observations of rhyolitic eruptions have revealed that degassed lava effusion may depend upon outgassing during simultaneous pyroclastic venting. The outgassing is thought to occur as gas and pyroclastic debris are discharged through shallow fracture networks within otherwise low-permeability, conduit-plugging lava domes. However, this discharge is only transient, as these fractures become clogged and eventually blocked by the accumulation and sintering of hot, melt-rich pyroclastic debris, drastically reducing their permeability and creating particle-filled tuffisites. In this study we present the first published permeability measurements for rhyolitic tuffisites, using samples from the recent rhyolitic eruptions at Chaitén (2008-2009) and Cordón Caulle (2011-2012) in Chile. To place constraints on tuffisite permeability evolution, we combine (1) laboratory measurements of the porosity and permeability of tuffisites that preserve different degrees of sintering, (2) theoretical estimates on grainsize- and temperature-dependent sintering timescales, and (3) H_2O diffusion constraints on pressure-time paths. The inferred timescales of sintering-driven tuffisite compaction and permeability loss, spanning seconds (in the case of compaction-driven sintering) to hours (surface tension-driven sintering), coincide with timescales of diffusive degassing into tuffisites, observed vent pulsations during hybrid rhyolitic activity (extrusive behaviour coincident with intermittent explosions) and, more broadly, timescales of pressurisation accompanying silicic lava dome extrusion. We discuss herein the complex feedbacks between fracture opening, closing, and sintering, and their role in outgassing rhyolite lavas and mediating hybrid explosive-effusive activity.

Keywords: lava dome; rhyolite; permeability; tuffisite; sintering; H_2O diffusion

1 Introduction

Unprecedented observations of recent subaerial rhyolite eruptions in Chile have demonstrated that effusive extrusion of rhyolitic lava can be coincident with intermittent explosions of ash, lapilli, and bombs (Castro et al., 2014; Lara, 2009; Schipper et al., 2013). Such hybrid activity demands reappraisal of existing paradigms of eruptive style transitions (Eichelberger et al., 1986) and highlights that outgassing mechanisms are of critical importance (e.g., Chevalier et al., 2017; Collinson & Neuberg, 2012; Farquharson et al., 2017; Gonnerman and Manga, 2003; Kushnir et al., 2017; Ryan et al., 2019). Chaitén volcano (Chile) exhibited prolonged hybrid activity in 2008 (Castro et al., 2014), whereas longer-lived hybrid (nine months) activity occurred at Cordón Caulle (also in Chile) during 2011-2012 (Schipper et al., 2013). In both cases pulsatory pyroclastic discharge occurred from fractures in vent-filling lava (Figure 1), a process now believed to have accompanied ancient silicic lava dome eruptions in other localities (e.g., Black et al., 2016). For example, the photograph taken during the January 10th 2012 activity at Cordón Caulle (t = + 4 s) shows that localised outgassing occurred via pathways with fracture (i.e. plane) geometries (Figure 1a), rather than outgassing through permeable foam (e.g., Eichelberger et al., 1986). Indeed, recent experimental work by Ryan et al. (2019) has shown that it is difficult to create permeability in initially impermeable, high-porosity foams, describing them as "persistently impermeable". Dense obsidian bombs emitted during hybrid activity characteristically hosted tuffisites, which are centimetric fractures infilled with pyroclastic material (Castro et al., 2012; Heiken et al., 1988; Saubin et al., 2016; Stasiuk et al., 1996; Tuffen et al., 2003; Figure 2a). Tuffisites have been interpreted to record the transient opening and occlusion of the permeable pathways that provide fleeting escape routes for pressurised gas prior to eventual blockage and violent ejection (Saubin et al., 2016). H_2O concentration gradients at the tuffisite-host rock interface (Castro et al., 2012; Berlo et al., 2013) and within fracture-filling clasts (Saubin et al., 2016) provide constraints on tuffisite depths (hundreds of meters), timescales of

fracture opening (tens of minutes to several hours), and gas pressure changes associated with fracture opening (reductions of up to several MPa).

Modelling approaches (e.g., Diller et al., 1996; Collinson & Neuberg, 2012) and field measurements (e.g., Stix et al., 1993) have shown a low-permeability magmatic plug in the upper conduit can render outgassing ineffective, promoting gas accumulation and pressurisation (a "closed system"). More recent modelling by Chevalier et al. (2017) has shown that, although the dome can increase the pressure on the system and reduce gas loss at the conduit walls, the permeability of the conduit walls is of greater importance that the permeability of the dome in controlling gas loss and pressurisation. In the case of a "closed system", the initially highly permeable fracture networks, thought to be ultimately recorded as tuffisites, must play a key role in mediating gas release and pressurisation cycles. Recent modelling by Farquharson et al. (2017), focused on the time-dependent permeability evolution of compacting fractured volcanic systems, defined three regimes: (1) an "outgassing" regime, where pore pressure does not increase during compaction; (2) a "diffusive relaxation" regime, where the ongoing reduction in porosity is compensated by the molecular diffusion of water and; (3) a "pore pressure increase" regime, where Darcian or diffusive processes cannot compensate for the porosity reduction and pore pressure builds. As improved modelling of conduit dynamics requires better constraints on the temporal evolution of tuffisite permeability, recent work has addressed the porosity and permeability of variably sintered pyroclastic material (Gardner et al., 2018; Heap et al., 2014, 2015; Kendrick et al., 2016; Kolzenburg & Russell, 2014; Okumura & Sasaki, 2014; Ryan et al., 2018a, 2018b; Vasseur et al., 2013) and provided models of compaction and viscous sintering (i.e. the agglutination of glassy particles held at or above their corresponding glass transition temperature; Farquharson et al., 2017; Russell and Quane, 2005; Wadsworth et al., 2014, 2016a, 2016b, 2017a). These recent data and modelling provide a blueprint for placing firmer constraints on permeability evolution within volcanic conduits.

We present herein porosity and permeability measurements for tuffisites hosted within dense obsidian bombs ejected from recent rhyolitic eruptions at Chaitén (2008-2009) and Cordón

Caulle (2011-2012). These data, which represent the first permeability measurements of rhyolite-hosted tuffisites, are combined with models for viscous sintering and pressure-timescale constraints from H_2O diffusion gradients to provide a detailed description of tuffisite permeability evolution, and thus explore the role of fracture-assisted outgassing within shallow silicic conduits.

2 Anatomy of a tuffisite

Three rhyolitic tuffisites (CH5F, BTB, and CH5G) hosted within decametric dense obsidian bombs that were ejected during hybrid activity in May 2008 at Chaitén volcano (an example is provided as Figure 2a) and found within the pyroclastic density current deposits about 800 m from the 2008-2009 vent were selected for this study. Several field campaigns at Chaitén volcano have highlighted that bombs on the crater rim and flanks commonly host tuffisites. The width of these tuffisites typically ranged from a couple of millimetres up to a few tens of millimetres. The tuffisites within these bombs comprise poorly sorted and variably sintered angular fragments of dense obsidian, pumice, and lithics within a fine ash-grade matrix (Figure 2a). The three samples chosen for this study were selected because of visible differences in density/porosity (photographs of core samples prepared from these three tuffisites are provided as Figures 2c, 2d, and 2e), suggesting underlying differences in their degree of sintering. As a result, we consider that these samples provide snapshots in time of the viscous sintering process. We complement these samples with a tuffisitic bomb fragment from Cordón Caulle, part of a decametric breadcrust bomb found 1.5 km NW of the vent (Figure 2b). The bomb was ejected between June 7th and 15th 2011, as the vent constricted prior to and during the onset of lava effusion and thus hybrid activity. It comprises glassy, tuffisitic material that has partly vesiculated after fragmentation, with inflation of the largest, most volatile-rich clasts (Figures 2b and 2f).

Backscattered scanning electron microscope (SEM) images of the four tuffisites were collected using a Tescan Vega 2 XMU system, and representative tuffisite textures are shown in Figures 3 and 4. The tuffisites comprise a similar population of ash- and lapilli-sized juvenile and lithic fragments (Figures 3 and 4). The juvenile fragments within the tuffisites are glassy and often

angular, but their edges can be rounded or diffuse, depending on the degree of viscous sintering. For example, the sintering of juvenile clasts in sample CH5F is sufficiently advanced that it is difficult to distinguish individual fragments (Figures 4a and 4b), with remaining porosity preferentially located at the margins of lithic clasts (Figure 4b). Viscous sintering is least well developed in sample CH5G, with individual glassy juvenile fragments often easily identifiable (Figure 4c and 4d). Indeed, the matrix porosity is noticeably higher in the CH5G sample than the other three samples and is not restricted to lithic clast margins (Figure 4c and 4d). Individual glassy particles in sample B1 appear rounded and are only distinguishable because of the interstitial pore space, which has been compacted and deformed (Figure 4f).

Some juvenile clasts in the BTB (Figure 3), CH5G (Figure 4d), and B1 (Figures 4e and 4f) samples have vesiculated centres leading to a frothed appearance. Quantification of vesicle size distributions and H_2O concentrations in sample BTB (Saubin et al., 2016) has facilitated a detailed reconstruction of the relative timing of clast vesiculation and fracture opening, together with the evolution of gas pressure in the system. Results show that, for sample BTB, the strongly vesiculated clasts had vesiculated prior to their incorporation into the fracture by pressurised gas from deeper in the conduit. However, it is likely that the common vesiculated juvenile clasts in sample B1 (Figure 4e) have predominantly vesiculated after bomb ejection. Vesiculated juvenile clasts are rare in sample CH5F (Figure 4a and 4b).

Lithic fragments in these tuffisites can be angular, but they are often sub-rounded (Figures 3 and 4). Most lithics are rhyolite fragments that are banded and microporous with cristobalite and minor plagioclase phases protruding into pore spaces (Figures 3 and 4). Finally, we highlight that the boundary between the tuffisite and the obsidian host rock is curvilinear on the microscale (Figure 3b). Further details on the clast population within the BTB tuffisite, including grainsize distribution and componentry, and the relationship between the timing of fracture opening and clast vesiculation, can be found in Saubin et al. (2016).

3 Experimental methods

159 Cylindrical samples (either 20 or 10 mm diameter) of the tuffisitic material were cored
160 from each bomb. Samples were cored such that their axis is parallel to the fracture plane, so as to
161 maximise the number of samples extracted from each of the blocks collected (see inset on Figure
162 2a). Samples from the Cordón Caulle bomb were prepared to avoid large vesiculated fragments
163 and the ~decametre-spaced cooling contraction fractures associated with breadcrusting (see
164 Figure 2b). We also prepared a 20 mm-diameter sample of the dense obsidian host rock from the
165 BTB bomb. These samples were precision-ground to lengths of 30-40 mm (for the 20 mm-
166 diameter samples) or 20-40 mm (for the 10 mm-diameter samples) and dried for a minimum of
167 48 h inside a vacuum oven at 40 °C. All samples were prepared such that their length-diameter
168 ratio is greater than one. Recent experiments by Heap (2019) highlighted that reliable laboratory
169 measurements of permeability are possible on small cores (e.g., 10 mm-diameter cores) as long
170 as the pore/grain size is small with respect to the core dimensions.
171 The connected porosity and permeability was then measured for each cylindrical sample.
172 The connected porosity of each sample was calculated using the bulk volume of the sample
173 (calculated using the sample dimensions) and the skeletal (i.e. connected) volume given by a
174 Micromeritics AccuPyc II 1340 helium pycnometer. The total porosity of each sample was
175 determined using the solid density of each block (measured using a hand-powdered aliquot of
176 each sample and the helium pycnometer) and the bulk sample density of each cylindrical sample
177 (calculated using the mass and dimensions of each sample). The isolated porosity of each sample
178 could then be determined by subtracting the connected porosity from the total porosity.
179 Permeability was measured using a gas (argon or nitrogen) permeameter following the operating
180 procedure given in Farquharson et al. (2016) and Heap and Kennedy (2016). Permeability was
181 measured under a confining pressure of 1 MPa (a confining pressure is needed to ensure that the
182 gas travels through the sample, rather than between the jacket and the sample edge) using the
183 steady-state method. The permeability of a sample of BTB was also measured under confining
184 pressures up to 10 MPa to cover the range of pressures inferred during tuffisite formation

(equivalent to 400-500 m lithostatic; Castro et al., 2014; Saubin et al., 2016) and using the same procedure described above.

To measure permeability, the volumetric flow rate, Q_v (in m^3/s) was measured using a gas flowmeter for several different pressure differentials, ΔP (we define ΔP as the upstream pore fluid pressure, P_u (in Pa), minus the downstream pore fluid pressure, P_d (in Pa)). In our permeameter setup, P_d is the atmospheric pressure (assumed to be 101325 Pa). The Darcian permeability, k_D (in m^2), was then determined for each of the pressure differentials using the following relationship for compressible gas:

$$k_D = \frac{Q_v}{P_m \Delta P} \frac{\mu L P_d}{A}. \quad (1)$$

Where μ is the pore fluid viscosity (viscosity of argon and nitrogen at 20 °C was taken as 2.22×10^{-5} and 1.76×10^{-5} Pa s, respectively; values taken from the National Institute of Standards and Technology, https://www.nist.gov/), A (in m^2) and L (in m) are the sample cross sectional area and the sample length, respectively, and P_m is the mean pore fluid pressure (i.e. $(P_u + P_d)/2$). We calculate k_D for a range of different pressure differentials (typically six) to assess whether fluid flow departs from Darican flow (i.e. Equation 1). We assume a constant pore fluid density and viscosity for our measurements, a valid assumption for the very low pressure differentials used in this study (the pressure differential never exceeded 0.5 MPa). Fluid flow can be complicated by gas slippage (the Klinkenberg effect; Klinkenberg, 1941) and/or by turbulence (the Forchheimer effect; Forchheimer, 1901). We first check whether a Forchheimer correction is needed. To do so, we plot $1/k_D$ for each pressure differential, ΔP, as a function of Q_v. If these data can be well described by a positive linear slope, the Forchheimer-corrected permeability k_{forch} is the inverse of the y-intercept of the best-fit linear regression of this relationship. If the Forchheimer correction is needed, it is then necessary to check whether the Klinkenberg correction is needed. To check whether the Klinkenberg correction is needed, we calculate k_{forch} for each pressure differential, ΔP, using the following relation:

$$\frac{1}{k_D} = \xi Q_v + \frac{1}{k_{forch}}. \quad (2)$$

Where the slope of the plot of $1/k_D$ as a function of Q_v is given by ξ. The Klinkenberg correction is needed if the data on a plot of k_{forch} as a function of $1/P_m$ can be well described by a positive linear slope. If this is true, the permeability is the *y*-intercept of the best-fit linear regression of these data. If the data cannot be well described by a positive linear relationship, the permeability is the inverse of the *y*-intercept of the best-fit linear regression on the plot of $1/k_D$ as a function of Q_v (i.e. k_{forch}). If the Forchheimer correction is not needed, we assess the need for the Klinkenberg correction by plotting k_D as a function of $1/P_m$. If the data can well described by a positive linear slope, a Klinkenberg correction is required and the permeability is the *y*-intercept of the best-fit linear regression on the graph of k_D as a function of $1/P_m$. If no corrections are needed, the permeability is taken as the positive slope of the plot of Q_v as a function the mean pore fluid pressure P_m multiplied by ΔP. These ancillary corrections were implemented on a case-by-case basis (we refer the reader to Heap et al. (2018a) for examples). The values of the coefficient of determination (R^2) for the best-fit regressions, when applied, were between 0.98 and 0.99, where a value of unity represents perfect agreement. A more detailed description of our permeability data analysis technique can be found in Heap et al. (2017).

To assess the size of the smallest pore apertures of a tuffisite, we performed mercury injection porosimetry on a piece (4.7 g) of the BTB sample using a Micromeritics Autopore IV 9500. The mercury equilibration time and filling pressure were 10 s and ~3585 Pa, respectively. The evacuation time and evacuation pressure were 5 min and 50 μmHg, respectively. The pressure range was ~690 Pa up to ~414 MPa. Data from a mercury injection test were used to calculate the pore throat size distribution of the sample (ASTM D4404-10, 2010). We corrected the mercury injection data for the "low pressure correction", as recommended by the American Society for Testing and Materials (ASTM D4404-10, 2010).

The dissolved H_2O concentration was measured along a profile from the boundary of the tuffisite in the CH5G sample (position of the profile is shown on an inset in Figure 6c) using synchrotron-source Fourier Transform infrared spectroscopy (SFTIR) at the Diamond Light Source (UK) MIRIAM beamline. A Hyperion 3000 microscope with a broadband MCT detector was coupled to a Bruker Vertex 80V FTIR interferometer with KBr beamsplitter. A 10 μm square aperture was used and 128 spectra were collected in transmission mode at 8 cm^{-1} spectral resolution between 4000-1000 cm^{-1}. Wafer thickness (average thickness of 90 μm) was measured using either a digital micrometer (precision ±3 μm) or by the reflection fringe method (von Aulock et al., 2014). Peak heights at 3550 cm^{-1} (H_2O_t) and 1630 cm^{-1} (H_2O_m) were determined using 18-point linear baseline corrections. Using the Beer-Lambert Law, a glass density of 2281 kg m^{-3} (Saubin et al., 2016), and absorption coefficients of 80 l mol^{-1} cm^{-1} (3550 cm^{-1}; Ihinger et al., 1994) and 55 l mol^{-1} cm^{-1} (1630 cm^{-1}; Newman et al., 1986; Okumura et al., 2003), we converted these data to species concentrations. The combined uncertainty of this method, which depends on the wafer thickness and density and the choice of molar absorption coefficient, is typically <10% (von Aulock et al., 2014). We compare these data with those already collected for the BTB sample (presented in Saubin et al., 2016) using the same technique.

4 Results

Connected porosity as a function of total porosity is shown in Figure 5a (data available in Table 1). The connected porosity of these tuffisites varies from ~0.05 to ~0.2 (Figure 5a; Table 1). All of the measured tuffisites contain isolated porosity. The three samples from Chaitén contain isolated porosities between ~0.01 and ~0.075, whereas the B1 sample from Cordón Caulle contains a very high isolated porosity of ~0.17-0.19 (Figure 5a; Table 1).

Permeability as a function of connected porosity is shown in Figure 5b (data available in Table 1). CH5G contains the largest connected porosity (~0.2) and has the largest permeability (~6×10^{-15} m^2). Although BTB and CH5F contain similar connected porosities (~0.07), BTB is approximately an order of magnitude more permeable (~3×10^{-15} m^2 compared to ~6×10^{-16} m^2;

Figure 5b; Table 1). The connected porosity of B1 is larger (up to ~0.12) than both CH5G and BTB, but has a permeability close to that of BTB (Figure 5b; Table 1). The porosity and permeability of the obsidian host were found to be within error of zero (Table 1). Data at elevated confining pressure show that tuffisite permeability does not change significantly up to 10 MPa (Figure 6a). The permeability of the BTB sample was reduced from 2.04×10^{-15} m^2 at a confining pressure of 1 MPa to 1.73×10^{-15} m^2 at a confining pressure of 10 MPa (Figure 6a; Table 1).

The data from the mercury injection experiment (Figure 6b) indicate that about 8% of the connected void volume is connected by pore throats that are >5 μm in radius, 72% of the connected void volume is connected by pore throats between 0.05 and 5 μm in radius, and 20% of the connected void volume is connected by pore throats <0.05 μm in radius.

In sample CH5F, the H_2O concentration is 0.46 wt.% at the tuffisite boundary and reaches a constant value of 1.04 wt.% at ~400 μm from the boundary (black symbols on Figure 6c). The H_2O concentration in the BTB sample (data from Saubin et al., 2016) is ~0.65 wt.% at the boundary of a vesicular clast and increases to ~0.9 wt.% at a distance of ~100 μm (grey symbols on Figure 6c).

5 Discussion

5.1 Isolated porosity within the tuffisites

Our data show that the all of the measured tuffisites contain isolated porosity (Figure 5a; Table 1). The high isolated porosity of these samples is due to the presence of vesiculated juvenile clasts, which typically contain glassy rim with a porosity and therefore permeability of zero (Figures 3 and 4). Sample B1, from Cordón Caulle, contains abundant vesiculated juvenile clasts (Figures 4e and 4f) and, as a result, contains the largest isolated porosity of ~0.17-0.19 (Figure 5a; Table 1). Since the porosity in these clasts is isolated (encapsulated within a zero porosity glassy rim; Figures 3 and 4), it does not therefore contribute to the permeability of the samples.

292 5.2 Permeability modelling: pore and grainsize analyses

293 The collected porosity and permeability data can be interrogated to better understand (1)
294 the average pore radius used by the gas molecules to travel through the tuffisite, and (2) the
295 particle size that likely controls the efficiency of viscous sintering.

296 First, we estimate of the average radius of the pores used by the gas molecules using the
297 Klinkenberg slip factor, b (a calculation only possible for the data that required a Klinkenberg
298 correction, see Table 1). Since the mean free path is inversely proportional to the mean pore fluid
299 pressure, Poiseuille's law for gas flow in a cylindrical tube and Darcy's law for flow in a porous
300 medium provide the following relation:

301

302 $$k_{klink} = k_D \left(1 + \frac{b}{P_m}\right). \quad (3)$$

303

304 Where k_{klink} is gas permeability corrected by the Klinkenberg correction (see the methods
305 section for details). Assuming a cylindrical pore shape, the average pore radius a used by the gas
306 molecules can then be estimated using the following relationship (Civan, 2010; Firouzi et al.,
307 2014):

308

309 $$a = \frac{4}{b}\eta\sqrt{\frac{\pi R_g T}{2M_w}}. \quad (4)$$

310

311 Where T is the temperature (293 K for room-temperature laboratory conditions), M_w is the molar
312 mass of the argon pore fluid (0.03995 kg mol^{-1}), and R_g is the ideal gas constant (8.31 J mol^{-1} K^{-1}).
313 This method has been used to estimate the average pore radius of the flow path in shales, (e.g.,
314 Firouzi et al., 2014; Heller et al., 2014; Letham and Bustin, 2015), volcanic rocks (Heap et al.,
315 2018a), and limestones (Heap et al., 2018b). We find an average pore radius of 0.75 μm for the
316 BTB sample at a confining pressure of 1 MPa (Figure 6a). The average pore radius estimated using
317 Equation (4) is reduced only slightly (to 0.70 μm) when the confining pressure is increased to 10

MPa (Figure 6a). The average pore radius estimated using the Klinkenberg slip factor highlights the complexity of the flow path within the BTB tuffisite. For example, although 40% of the void space within the tuffisite is connected by pore throats with a radius greater than 1 μm (Figure 6b), the gas travels through narrow microstructural elements (with a radius < 1 μm). Because the permeability and the average pore radius used by the gas do not vary considerably with pressure (Figure 6a), it is likely that these narrow microstructural elements are the tortuous inter-granular pores characteristic of sintering systems (microcracks are easily closed as confining pressure is increased; e.g., Nara et al., 2011). These data therefore highlight that our measurements at 1 MPa are relevant for *in-situ* tuffisites and that their compressibility is low even under relevant upper conduit pressures.

Wadsworth et al. (2016a) provide a model for predicting first the characteristic lengthscale of the pore network, $1/s$, and second the permeability, k_D, of sintered granular materials for which the inter-grain spaces are the pore network. The modelled permeability is given by (Wadsworth et al., 2016a):

$$k_D = \frac{2[1-(\phi-\phi_c)]}{s^2}(\phi-\phi_c)^{\bar{e}}, \quad (5)$$

where s is the specific surface area, i.e. the ratio of pore surface area within the sample to the sample volume (in m^{-1}), ϕ_c is the porosity of the percolation threshold at which the permeability can be considered zero, and $\bar{e}$ is a percolation exponent. As noted by Wadsworth et al. (2016a), this model has the appealing features that the permeability falls to zero as $\phi \to \phi_c$, and for all ϕ above ϕ_c, it has a power-law dependence on ϕ, for which the exponent is $\bar{e}$, similar to theoretical constraints (Feng et al., 1987). Feng et al. (1987) constrained $\bar{e} = 4.4$ based on theoretical scaling, while empirical fits to a large range of data collected for variably welded granular rocks yield $\bar{e} = 4.2 \pm 0.3$ (Wadsworth et al., 2016a). ϕ_c is typically around 0.03 for initially granular systems (Rintoul et al., 2000; Wadsworth et al., 2016b). The specific surface area is then related to the pore radius via $s = 3(1-\phi)\ln(1-\phi)/a$ assuming that the pore network can be approximated as a

pack of overlapping spherical pores (see Torquato, 2013). Finally, the pore radius a is predicted at the initial packing porosity ($\phi_i = 0.5$) from the grainsize distribution, using the mean of the distribution $\langle R \rangle$ and the porosity after Torquato and Avellaneda (1991), with the full solution provided in Wadsworth et al. (2016a). We then compare the modelled permeability curves (using Equation 5), solved for a range of mean grainsize $\langle R \rangle$, with our porosity and permeability measurements for the tuffisite samples (Figure 5b). The measured porosity and permeability data are consistent with initial grain radii of $2.5 < \langle R \rangle < 15$ μm (Figure 5). Although these inferred radii are small compared to the fragments readily identifiable in our microstructural work (Figures 3 and 4), they are consistent with previous measurements of the fine fraction that dominates the matrix in the BTB sample (Saubin et al., 2016). This range of predicted grainsizes is therefore likely to represent the grainsize that controls the efficiency of viscous sintering—a result of the inverse grainsize dependence of the sintering rate (Wadsworth et al., 2014). The grainsizes predicted using this approach are similar to those predicted for similar variably sintered, granular volcanic material (welded block-and-ash flow deposits, BAF, from Mt. Meager in Canada; data taken from Heap et al., 2015), shown as light grey-coloured circles in Figure 5b.

Next we use an empirical fitting procedure to predict the pore radii for each tuffisite. We assume that Equation (5) is a valid description of the permeability as a function of the porosity, and that $\bar{e} = 4.2$ and $\phi_c = 0.03$. We use the Excel Solver tool to minimise for a single controlling value of s for each sample and to assess the uncertainties that result using the method outlined in Kemmer and Keller (2010). This yields a fitted s that can be converted to a mean pore radius characteristic of flow through the sample using the above $s(a, \phi)$ result. The output is $a = 2.5 \pm 0.9$ μm for the BTB sample, and $a = 1.0 \pm 0.4$ μm for the CH5F, CH5G, and B1 samples. This provides a natural method to normalise the permeability by $ks^2/(2[1 - (\phi - \phi_c)])$. In Figure 7 we demonstrate that this method results in a collapse of the data to a single permeability description that is consistent with both $4.2 < \bar{e} < 4.4$, as predicted by theory (Feng, 1987; Wadsworth et al., 2016a, 2017b). We also plot the welded block-and-ash flow data from Heap et al. (2015) and the data for tuffisites found on the dome of Volcán de Colima, an andesitic

stratovolcano in Mexico (permeability measured using the TinyPerm II field permeameter; Kendrick et al., 2016). These data also collapse on our permeability description (Figure 7). Additionally, the pore radii resulting from this method (1-2.5 μm) are within a factor of 2 of those calculated from the Klinkenberg factor (0.7-0.75 μm) and within the range measured by mercury injection porosimetry (Figure 6b).

The above approach provides several methods for predicting the controlling lengthscales for fluid flow through samples of this type, including direct measurements. We have shown that use of Equation (5) results in good collapse of the data (and data for other welded volcanic materials and tuffisites from Mt. Meager and Volcán de Colima, respectively; Figure 7) to a single dimensionless description, which lends confidence to the generality of this model. We propose that this may be a useful tool for predicting the permeability decay of evolving tuffisites as they sinter and heal in silicic volcanoes.

5.3 H_2O diffusion modelling

Modelling the depletion in H_2O adjacent from the tuffisite-host rock boundary, or from the boundary of a vesicular clast within the tuffisite, provides an estimate of the time between fracture filling and final quenching (e.g., Castro et al., 2012). Our modelling of the H_2O diffusion profiles employed an error-function solution to Fick's general diffusion equation cast in 1D Cartesian coordinates for a constant diffusivity (after Crank, 1979):

$$\frac{c_x - c_b}{c_0 - c_b} = 1 - \mathrm{erf}\left[\frac{x}{2\sqrt{Dt}}\right]. \quad (6)$$

Where c_x denotes the concentration of H_2O (in wt.%) at a distance of x from the fracture/clast boundary (m), c_b is the H_2O concentration of the far-field in the host obsidian (in wt.%), c_0 is the (lower) H_2O concentration within the tuffisite defining the limit at the tuffisite wall (in wt.%), t is time (s), and the H_2O diffusivity ($m^2 s^{-1}$) is given by D. H_2O molecules were assumed to be the only species diffusing (e.g., Behrens & Nowak, 1997) and the magmatic temperature was assumed to

398 be constant at 825 °C (a value constrained by the petrological experiments of Castro & Dingwell,
399 2009). Boundary conditions were fixed at the far-field H_2O concentration c_0, as defined from
400 diffusion profiles, and the lowest H_2O concentration c_b as measured at the fracture/clast
401 boundary. The H_2O diffusivity was calculated using the concentration- and temperature-
402 dependent model for rhyolitic melt of Zhang (1999):
403
404 $$D_{H_2O_t} = \left(\frac{c}{c_r}\right)\exp\left[-16.83 - \frac{10992}{T}\right], \quad (7)$$
405
406 where c is the local H_2O concentration (in wt.%), c_r is a reference H_2O concentration of 1 wt.% (see
407 Figure 6c and Zhang (1999)), and T is the temperature (K). As the error function diffusion solution
408 assumes a constant diffusivity, which we take to be the diffusivity calculated using Equation 7 for
409 a value of $c = 0.75$ wt.%, which is the arithmetic mean of the measured c_0 and c_b (yielding $D_{H_2O_t}$ =
410 1.6×10^{-12} m^2s^{-1}). Because the difference between diffusivities at c_0 and c_b is modest (1×10^{-12} m^2s^{-1} at 0.46 wt.% H_2O, and 2.3×10^{-12} m^2s^{-1} at 1.04 wt.% H_2O), using this mean value provides a
412 reasonable approximation of the diffusivity over the whole profile. We note that taking the mean
413 of the two end-member diffusivities additionally assumes that the non-linearity of $D_{H_2O_t}(H_2O_t)$ is
414 negligible. Using this method and fitting the diffusion model to the measured H_2O depletion
415 adjacent to the fracture/clast boundary of the CH5F and BTB tuffisites with the time as an
416 adjustable parameter (and fitting using a least squares minimisation method described above)
417 yields times of ~4 and ~2 h, respectively, for the time between fracture opening and final
418 quenching (Figure 6c). It is important to highlight these timescales are *minima*, and they depend
419 heavily on the model assumptions, such as the temperature. For example, Castro et al. (2012)
420 showed that reducing the temperature by 200 °C increased this timescale from minutes to several
421 tens of hours. Nevertheless, these predicted timescales compare well with other estimates of the
422 lifetimes of tuffisites from Chaitén volcano (Castro et al., 2012).
423

5.4 The lifespan of a tuffisite

In the general conceptual scheme explored here, we envisage conduit-filling rhyolite lava that is periodically fractured by high-pressure gas and ash from below (e.g., Schipper et al., 2013). These processes involve the opening of the fracture, the transport of gas and ash, the clogging of the fracture, and a slower, time-dependent sintering of the fracture infill. In concert then, the outgassing time available for removing pressurised gas through the fractures is therefore the sum of the time from opening to clogging with pyroclastic debris, λ_1, and the time for sintering once the tuffisite is formed and welds shut, λ. The time λ_1 from video footage of fractures opening and closing appears to be on the order of tens of seconds (Figure 1). The mass of gas and ash removed during this time, which could be used to compute the pressure decrease, is difficult to assess. But it is clear from the video footage (Figure 1; Schipper et al., 2013) that the outgassing continues, albeit more slowly, during the post-clogging sintering of the fracture infill, with the emission of vapour only (i.e. without the ash phase).

Once the fracture has become clogged with pyroclastic debris, the process of sintering will act to reduce porosity and permeability towards zero. It is the timescale of sintering that is the key quantity in determining the efficacy of tuffisites as outgassing pathways after the open fracture is clogged with particles. In the absence of applied force on the sides of the fracture, the characteristic timescale associated with this process is the sintering timescale $\lambda = \langle R \rangle \mu / \Gamma$, where μ is the viscosity of the melt and Γ is the melt-vapour surface tension. $\langle R \rangle$, the mean grainsize, has been shown to capture sintering dynamics even in highly polydisperse distributions (Wadsworth et al., 2017a). In other words, although estimates of $\langle R \rangle$ are small compared to the larger fragments readily identifiable in our microstructural work (Figures 3 and 4), it is the finer particle fraction that dictates the efficiency of viscous sintering—a result of the grainsize dependence of the sintering time (Gardner et al., 2018; Wadsworth et al., 2014; 2016b). When a force is applied to the fracture walls (such as a lithostatic pressure or the stress imparted by a recently opened adjacent fracture), however, λ will not be the controlling timescale, and the system is more likely to close over a compaction timescale $\lambda_2 \approx \mu/(\sigma\alpha)$, where σ is the applied stress (in Pa) on the

fracture walls, and α is an empirical factor (Farquharson et al., 2017; Quane et al., 2005) that was calibrated for sintering polydisperse particles similar to the tuffisites studied here (the block-and-ash flow deposits from Mt. Meager; Figure 5) to be $\alpha \approx 2$ (Heap et al., 2014). This is broadly similar to other compaction timescale approximations (Kennedy et al., 2016; McKenzie, 2011). If surface tension stress $2\Gamma/\langle R\rangle$ dominates over the stress applied to the fracture walls σ, then λ should be used. If instead the opposite is true, and the fracture wall stress dominates the surface tension stress, then λ_2 should be used. In each respective case, the total outgassing time is $\lambda_1 + \lambda$ or $\lambda_1 + \lambda_2$.

To illustrate how λ and λ_2 vary, we take $\Gamma = 0.3$ N/m for moderately dry rhyolites (Gardner & Ketcham, 2011). We note that Γ is significantly lower in rhyolites with up to ~4 wt.% dissolved water, but there are no measurements in the intermediate range of water contents, and these rhyolites are erupted close to the dry limit (Castro et al., 2014; Saubin et al., 2016). The melt viscosity of tuffisites from Chaitén (samples BTB and CH5F) and Cordón Caulle (sample B1) can be estimated using a multicomponent viscosity model (Giordano et al., 2008), using major element composition (using the compositions provided in Castro and Dingwell (2009) for Chaitén and in Alloway et al. (2015) for Cordón Caulle), an inferred eruptive temperature of 825 °C for Chaitén (Castro & Dingwell, 2009) and 890 °C for Cordón Caulle (Castro et al., 2013; Alloway et al., 2015), and measured H_2O concentrations. H_2O concentrations of 0.74 and 0.34 wt.% were taken for, respectively, the host obsidian and tuffisite in the BTB sample (Saubin et al. (2016), and 1.04 and 0.46 wt.% were taken for the host obsidian and tuffisite in the CH5F sample (see Figure 6c)). For the B1 sample, measurements on eruptive products from the 2012-2013 Cordón Caulle eruption provided a range of H_2O concentration between 0.1 and 0.5 wt.% (Militzer, 2013). The resulting viscosity range estimations were calculated to be $10^{8.05} < \mu < 10^{9.07}$ Pa s for the BTB sample, $10^{7.64} < \mu < 10^{8.65}$ Pa s for the CH5F sample, and $10^{7.15} < \mu < 10^{8.23}$ Pa s for the B1 sample.

We assume, given the relationship between sintering timescale and grainsize (Wadsworth et al., 2014), that the viscosity of the fine-grained matrix controls viscous sintering. For the variability in $\langle R\rangle$ predicted here ($2.5 < \langle R\rangle < 15$ μm; Figure 5b), sintering times in the absence of

applied forces λ are between 6 min and 5 h, between 16 min and 13.6 h, and between 2 min and 2.4 h for CH5F, BTB, and B1 respectively (Figure 8). To compute λ_2, as a first-order estimate we take $\sigma = 2$ MPa, which is computed by matching the solubility of water (assuming 100% of the pressure is water vapour pressure) based on Liu et al. (2005), to the value measured at the tuffisite wall c_0. This yields values of λ_2 (for the variability in $\langle R \rangle$ predicted here) between 11 s and 2 min, between 28 s and 5 min, and between 3.5 s and 42 s for CH5F, BTB, and B1 respectively (Figure 8). We again highlight that these timescales depend on the model input parameters: differences in viscosity (resulting from changes to the eruptive temperature and/or the water content, for example) can significantly modify these predictions. We also plot on Figure 8 an estimated range for the time from fracture opening to clogging with pyroclastic debris, λ_1 (10-20 s, estimated using available video footage form Cordón Caulle; Figure 1; Schipper et al., 2013) and the inter-fracture timescale ($\lambda_1 + \lambda$ or $\lambda_1 + \lambda_2$) (20-120 s; Schipper et al., 2013). These observed timescales are faster than the timescales solely predicted from surface tension and are much more consistent with the estimated range of compaction timescales (Figure 8), suggesting that compaction driven by the overburden (lithostatic) stress plays a key role in governing the lifetimes of these tuffisites. Although depth estimations for tuffisites at Cordón Caulle are shallower (depth of about 50 m; Schipper et al., 2013) than those estimated for Chaitén, we note that a reduction in σ from 2 to 1 MPa only doubles the λ_2 timescale and, even in this scenario, our estimated compaction timescales are still in line with the observed timescales. We further note that our estimated compaction timescales consider lithostatic pressures only and do not take stresses imparted by recently opened adjacent fractures into account.

H_2O diffusion offers an independent tuffisite chronometer to these estimated viscous sintering timescales. The best-fit diffusion model (Figure 6c) to the measured H_2O depletion adjacent to the fracture/clast boundary of the CH5F and BTB tuffisites yields timescales λ_d (time between fracture opening and final quenching) of ~4 and ~2 h, respectively (as shown in the previous section). These predicted timescales compare well with other estimates of the lifetimes of tuffisites from Chaitén volcano and elsewhere (Berlo et al., 2013; Cabrera et al., 2011; Castro et

al., 2012; Saubin et al. 2016). Further, we highlight that viscous sintering timescales were also found to coincide with H_2O re-equilibration timescales in obsidian pyroclasts from Mono Craters (USA) that were assembled from juvenile particles during magma ascent (Gardner et al., 2017), suggesting that viscous sintering plays an important role in cyclic fragmentation behaviour and apparent open-system degassing (Gardner et al., 2017; Rust et al., 2004; Tuffen et al., 2003; Watkins et al., 2017). Our predicted H_2O diffusion timescales are, however, longer than the observed inter-fracture timescales and the timescales predicted for compaction-driven sintering (Figure 8). Because H_2O diffusion can continue even after compaction renders permeable gas flow ineffective, we consider that λ_d is the sum of the fracture opening timescale (λ_1), the sintering or compaction timescale (λ or λ_2), and a quenching timescale. According to our analysis, the quenching timescale is therefore likely to be on the order of a couple of hours, consistent with conductive cooling of bombs tens of centimetres in diameter (e.g., Saubin et al., 2016). We also highlight the numerous model assumptions that may influence our predicted H_2O diffusion timescales, such as, for example, using a steady eruptive temperature and a single step in H_2O activity at the fracture walls. Furthermore, observations at Cordón Caulle highlight that ash jetting can occur from the same fracture and, since H_2O diffusion would necessarily continue, the repeated use of the same fracture could also help explain the discrepancy between the H_2O diffusion timescales and the timescales required for compaction, pressurisation, and fragmentation.

5.5 Pressurisation and outgassing at silicic lava flows and domes

Before discussing the potential role of tuffisites in influencing conduit processes and outgassing during silicic eruptions, it is important to address the question: how common are tuffisites? Providing a robust answer to this question for active volcanoes such as Chaitén or Cordón Caulle is problematic, in part because fully mature, densely welded tuffisite is likely indistinguishable from dense obsidian (see Castro et al., 2014). Calculations presented in Castro et al. (2012) suggest that a dense spacing of tuffisites (approximately a tuffisite every 0.01-0.001

m) would be required to fully degas a silicic magma in the approximate times available. Such high tuffisite number densities are considered consistent with evidence that obsidian lavas have been thoroughly fractured and then re-healed (or annealed) to dense glass (Castro et al., 2012, 2014). Further, several field campaigns at Chaitén volcano have highlighted that bombs on the crater rim and flanks commonly host tuffisites, the width of which typically ranged from a couple of millimetres up to a few tens of millimetres. Evidence of high tuffisite number densities from dissected rhyolitic conduits in Iceland (McGowan, 2016) provides support to the high densities predicted for Chaitén volcano by Castro et al. (2012). For example a 5 m line transect in a dissected rhyolitic conduit in Iceland contained 282 tuffisites (McGowan, 2016). Although the tuffisite number density from this dissected conduit may contains different generations of tuffisites (i.e. all 282 tuffisites may not have been active at the same time), this number speaks to the ubiquity, and therefore potential importance, of these features in rhyolitic conduits. We also note that, even if tuffisites are relatively uncommon, their influence on the permeability of an otherwise impermeable magmatic plug can be very large. For example, a single permeable pathway within an large low-permeability rock mass can increase the equivalent permeability of the system by many orders of magnitude, as discussed in, for example, Heap and Kennedy (2016), Farquharson et al. (2017), and Farquharson and Wadsworth (2018). Finally, although the outgassing flux could be computed using either Darcy law (low Reynolds number) or the Forchheimer equation using the constraints of permeability provided herein, we note that while our determination of the porosity-permeability relationship is valid locally, the depth-dependent stress and the coupling between the evolving gas pressure and the sintering rates demands a full numerical solution (e.g., Michaut et al., 2013). We propose that fertile future research could use our model, validated using empirical data on tuffisites, to provide a tuffisite outgassing model for rhyolitic volcanoes.

In upper conduits characterised by dense, impermeable magmatic plugs and host rock (i.e. a “closed system”; see the modelling of Diller et al., 2006; Collinson & Neuberg, 2012), we propose here that the recurrence timescale of explosive venting must, in a broad sense, equal the sum of the timescales of tuffisite sintering, pressurisation, and fragmentation. Our study provides

559 estimates spanning seconds (in the case of compaction-driven sintering) to hours (in the case of
560 surface tension-driven sintering) for the thorough sintering of tuffisites and we can assume that
561 the timescale for fragmentation is necessarily small compared to the other timescales. The
562 timescale for pressurisation, which will depend on, among other factors, the ascent rate and
563 volatile budget of the magma, is the missing constraint. Therefore, the sintering times estimated
564 herein must be less than or equal, and cannot be longer, than the explosive venting timescale.
565 Indeed, the observed range of cyclic pressurisation and ash venting timescales at erupting silicic
566 lava domes at, for example, Santiaguito volcano (Guatemala) and Soufriere Hills volcano
567 (Montserrat; Holland et al., 2011; Johnson et al., 2008; Voight et al., 1999), is consistent with our
568 timescale estimates for the thorough sintering of tuffisites. This may imply that pressurisation
569 timescales can be short or, and perhaps more likely, that pressurisation begins before the tuffisites
570 are completely sintered shut. Indeed, the presence of an H_2O-rich clast population within the BTB
571 sample demonstrated that deeper, pressurised gas entered the shallower, lower-pressure fracture
572 system, consistent with the pressurisation of fractures/tuffisites prior to the destruction of their
573 permeability.

574 The low permeabilities attained by the CH5F ($\sim 10^{-16}$ m^2; Figure 5b and Table 1) and the
575 BTB tuffisites ($\sim 10^{-15}$ m^2; Figure 5b and Table 1) coincide with that of healed gas escape routes
576 modelled by Collinson and Neuberg (2012). We consider that the effective healing of tuffisites
577 likely therefore contributed to the upper conduit pressure accumulation that ultimately led to
578 their explosive ejection. Although clast vesiculation contributed to porosity loss within the BTB
579 tuffisite (alongside other mechanisms), the BTB tuffisite failed to attain the low permeability of
580 CH5F, interpreted here as the result of a shorter pre-ejection healing time within the conduit.
581 Nonetheless, the permeability attained by BTB ($\sim 10^{-15}$ m^2) must have been sufficiently low to
582 render gas loss inefficient over its lifespan (pressure equilibrium time at this permeability >11
583 days; see also the modelling of Collinson & Neuberg, 2012; Chevalier et al., 2017). We note that it
584 is also possible that a healed tuffisite is not immediately ejected and undergoes additional viscous
585 compaction prior to ejection in a later fragmentation event – a plausible scenario given the

repetitive nature of tuffisite formation and healing (Tuffen et al., 2003). In this scenario, we would expect the diffusion timescale to greatly exceed the sintering timescale.

The modelled source depths of upper conduit pressurisation are additionally consistent with ejected bomb depths at Chaitén volcano, as inferred from bomb volatile concentrations (see above and Saubin et al., 2016). It is therefore plausible that upper conduit pressurisation cycles are modulated by sintering-driven blockage of initially permeable tuffisite networks, especially in crystal-poor rhyolitic systems where melt-rich magma readily sinters. Equivalent observational data from the 2008 eruption of Chaitén volcano is unfortunately lacking, but the filming of pulsatory ash venting during the eruption of Cordón Caulle in 2011-2012 revealed significantly shorter inter-explosion intervals (<40 s, Schipper et al., 2013; Figure 1), perhaps controlled by the sintering of finer material. The rhyolite at Cordon Caulle is also of lower silica content than Chaitén volcano and was erupted at comparatively higher temperatures (~890 °C; Castro et al., 2013), factors that reduce melt viscosity and therefore sintering timescales (e.g., Gardner et al., 2018; Figure 8). Nonetheless, limited video footage prior to the onset of the hybrid phase at Chaitén volcano in 2008 (Figure 1b) records a key phase of eruption development, in which the initially broad pyroclastic vent had constricted to several distinct vents tens of metres across above the yet-to-emerge lava dome (also observed at Cordón Caulle). Such focusing of pyroclastic discharge requires sintering of initially loose pyroclastic vent-filling material to gain strength and reduce permeability (e.g., Heap et al., 2015; Kolzenburg et al., 2012; Kolzenburg & Russell, 2014). This indicates that sintering processes can act to reconfigure conduit architecture during eruptions, and the transition from initially Plinian to hybrid activity at Chaitén volcano can be conceptualised as a decrease in the width of venting tuffisites from the entire conduit, through an intermediate phase characterised by multiple vents tens of metres in breadth, to, finally, pathways only centimetres wide such as observed in the BTB tuffisite (Figure 2a). Occlusion of outgassing pathways by sintering encourages greater pressurisation of the upper conduit, and this is proposed to be responsible for the forceful intrusion of a shallow laccolith at Cordón Caulle, whose

612 emplacement coincided with a marked narrowing of the vent prior to the onset of hybrid activity
613 (Castro et al., 2016).

614 The variable initial particle radius of a tuffisite relates to the efficiency of fragmentation
615 (Kueppers et al., 2006), together with sorting phenomena associated with clastic transport and
616 deposition (Tuffen et al., 2003). Fowler and Scheu (2016) demonstrate that, for a given porosity,
617 a larger overpressure release at fragmentation results in a smaller average grainsize. Owing to the
618 fact that viscous sintering timescales are shorter at small grainsizes (Gardner et al., 2018;
619 Wadsworth et al., 2014, 2016b), we conclude that violent decompression events associated with
620 fracture opening will create tuffisites capable of more rapid healing (for a given melt viscosity).
621 As healing can provoke repressurisation and explosive failure, the most energetic venting likely
622 involves the shortest duration cycles of pyroclast and gas ejection from fracture systems.

623 The accuracy of the calculations presented herein invariably rest on the accuracy of the
624 numerous model input parameters (such as the inferred temperatures used in our H_2O diffusion
625 modelling and viscosity calculations) and, therefore, although we consider our assumptions as
626 well reasoned, the model predictions should still be treated with some caution. Further
627 outstanding complications include the time evolution of particle viscosity during sintering as
628 diffusive mass transport of water occurs in tuffisites (Castro et al., 2014), grainsize sorting during
629 transport and accumulation of clastic particles (Tuffen & Dingwell, 2005), frictional heating and
630 its potential role as a sintering accelerant, the entrainment of cooler lithics into tuffisites (although
631 we highlight that lithics represent a very small fraction of the total fracture fill; for example, Saubin
632 et al. (2016) found that the lithic content of the BTB sample was <0.5 vol.%), and the effect of high
633 particle-particle pressures in pore networks exceeding the capillary pressures of sintering
634 (Wadsworth et al., 2016b). We further note that the tuffisites documented here are also end-
635 members in that they are hosted in dense obsidian; tuffisites in other systems characterised by a
636 more permeable host rock may behave, and be preserved, differently (e.g., tuffisites in a
637 pumiceous rhyolite host rock: Castro et al., 2012; the fractures documented at Volcán de Colima:
638 Farquharson et al., 2016; Kendrick et al., 2016; Kolzenburg et al., 2012; or the fractures seen

within pyroclasts from Katla, Iceland: Owen et al., 2019). Nevertheless, even in this scenario it is likely that the initially granular fracture fill will be of a higher permeability than the host rock. Therefore, although outgassing can occur through the host rock, we suggest that sintering timescales will be similar to those reported herein for rhyolitic systems and that tuffisites that form within a more permeable host rock will still play an important role in the cyclic bleeding and accumulation of pore pressure thought to drive episodic explosive events at active volcanoes. Indeed, connectivity between pumice-hosted tuffisites and exsolved gas in their vesicular walls can greatly facilitate outgassing and may be a key process assisting the formation of dense, compacted magma in shallow silicic conduits.

6 Concluding remarks

We conclude that if fractures in silicic lavas, domes, and vents are primary outgassing pathways for local and deep-seated magma (Castro et al., 2014), then the longevity of open-system outgassing from those fractures will scale with the timescale of viscous sintering. Our analyses suggest that it is the timescale for sintering driven by compaction that provides the most realistic timescale estimates and is likely therefore an important process dictating the lifespan of these tuffisites. Importantly, the permeability of those fractures will decay toward zero over that same timescale, rendering outgassing ineffective and permitting the pore pressure to build, eventually driving subsequent explosions and rapid concomitant lava extrusion rates (e.g., Pallister et al., 2013). The grainsize dependence of viscous sintering (Gardner et al., 2018; Wadsworth et al., 2014, 2016b) suggests that the most energetic venting (i.e. the most efficient fragmentation; Kueppers et al., 2006) likely involves shorter duration cycles of pyroclast and gas ejection from fracture systems. The first-order constraint on lava and lava dome permeability evolution presented herein could be used to compare with cycles of proximal geophysical and geochemical signals such as conduit inflation, low-frequency seismicity, and surface emissions of gas and ash.

Acknowledgements and Data

M.J. Heap and H. Tuffen are indebted to the Royal Society International Exchanges program for funding our project entitled “Volcanic valves: The permeability of tuffisites”. H. Tuffen was additionally supported by a Royal Society University Research Fellowship and thanks Lancaster University Sports Centre and grounds staff for assistance. J.M. Castro thanks support from the VAMOS research center, University of Mainz. The first author acknowledges funding from an Initiative d’Excellence (IDEX) “Attractivité” grant VOLPERM (funded by the University of Strasbourg). We also thank Bertrand Renaudié, Jamie Farquharson, Jérémie Vasseur, Ed Llewellin, Alexandra Kushnir, and Pauline Harlé. Gilles Morvan is thanked for technical support. The data collected for this study can be found in Table 1. The comments of two anonymous reviewers, the associate editor, and the editor helped improve this manuscript.

677 **Figures**

678

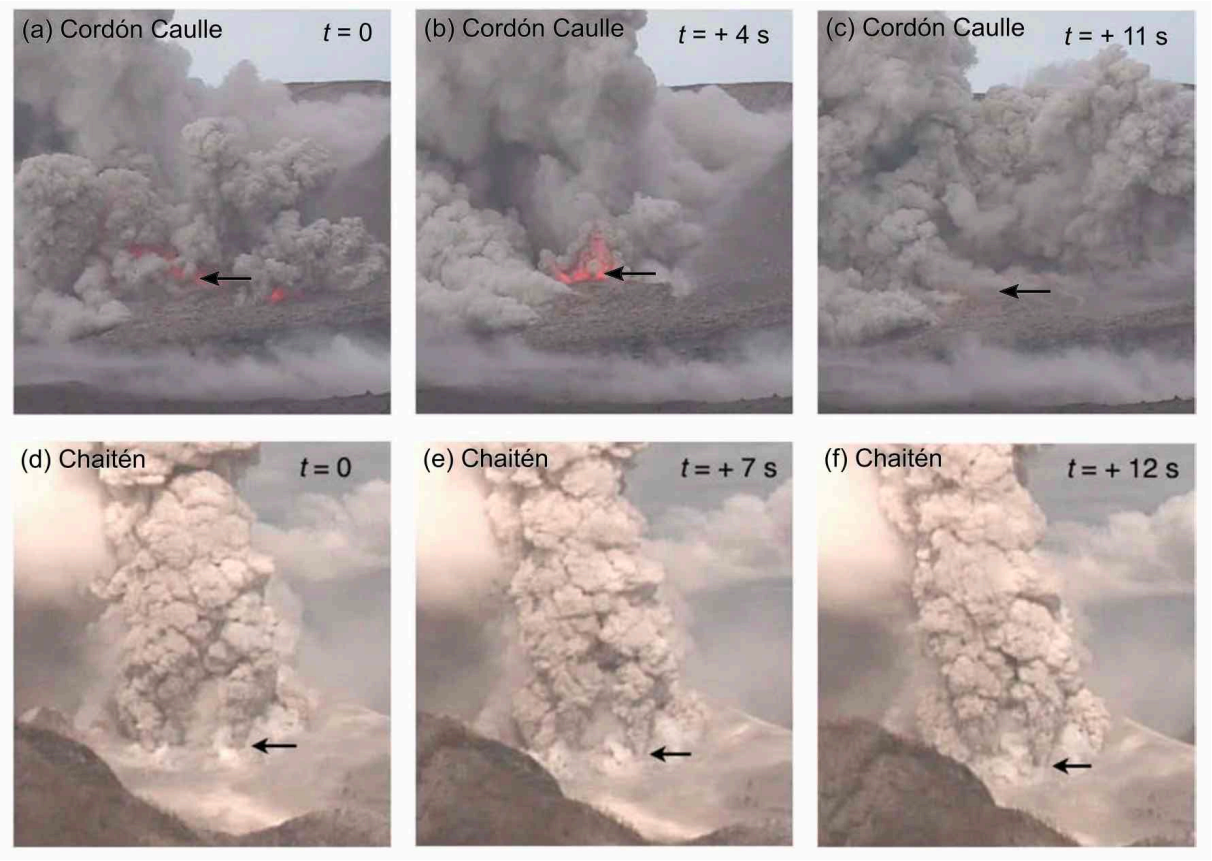

679

680 **Figure 1.** Explosive ash venting at (a) Cordón Caulle (January 10th 2012) and (b) Chaitén (May
681 10th 2008). (a) $t = 0$ ash venting from a newly opened fracture (indicated by the arrow). $t = 4$ ash
682 venting reaches a climax. $t = 11$ ash venting from the fracture has stopped, highlighting the
683 transient, pulsatory nature of the process. See also Schipper et al. (2013). (b) The time-stamped
684 Chaitén frames illustrate the formation of a funnel shaped ash jet indicated by the arrow (scale
685 100 m). This jet is one of many pyroclastic vents that emanate from a lava plug that will days later
686 form a voluminous obsidian dome.

Figure 2. (a) Photograph of a large bomb in the crater of the 2008 Chaitén eruption containing a tuffisite (the parent of the BTB block). The BTB tuffisite is 30 mm wide with remarkably planar walls. It is connected to a network of sub-millimeter subsidiary tuffisites in the dense obsidian host material (Saubin et al., 2016). (b) Photograph of the decametric breadcrust bomb from the June 2011 hybrid activity at Cordón Caulle. (c) Photograph of a 20 mm-diameter cylindrical sample of tuffisite CH5F (Chaitén). (d) Photograph of a 20 mm-diameter cylindrical sample of tuffisite BTB (Chaitén). (e) Photograph of a 10 mm-diameter cylindrical sample of tuffisite CH5G (Chaitén). (f) Photograph of a 20 mm-diameter cylindrical sample of tuffisite B1 (Cordón Caulle).

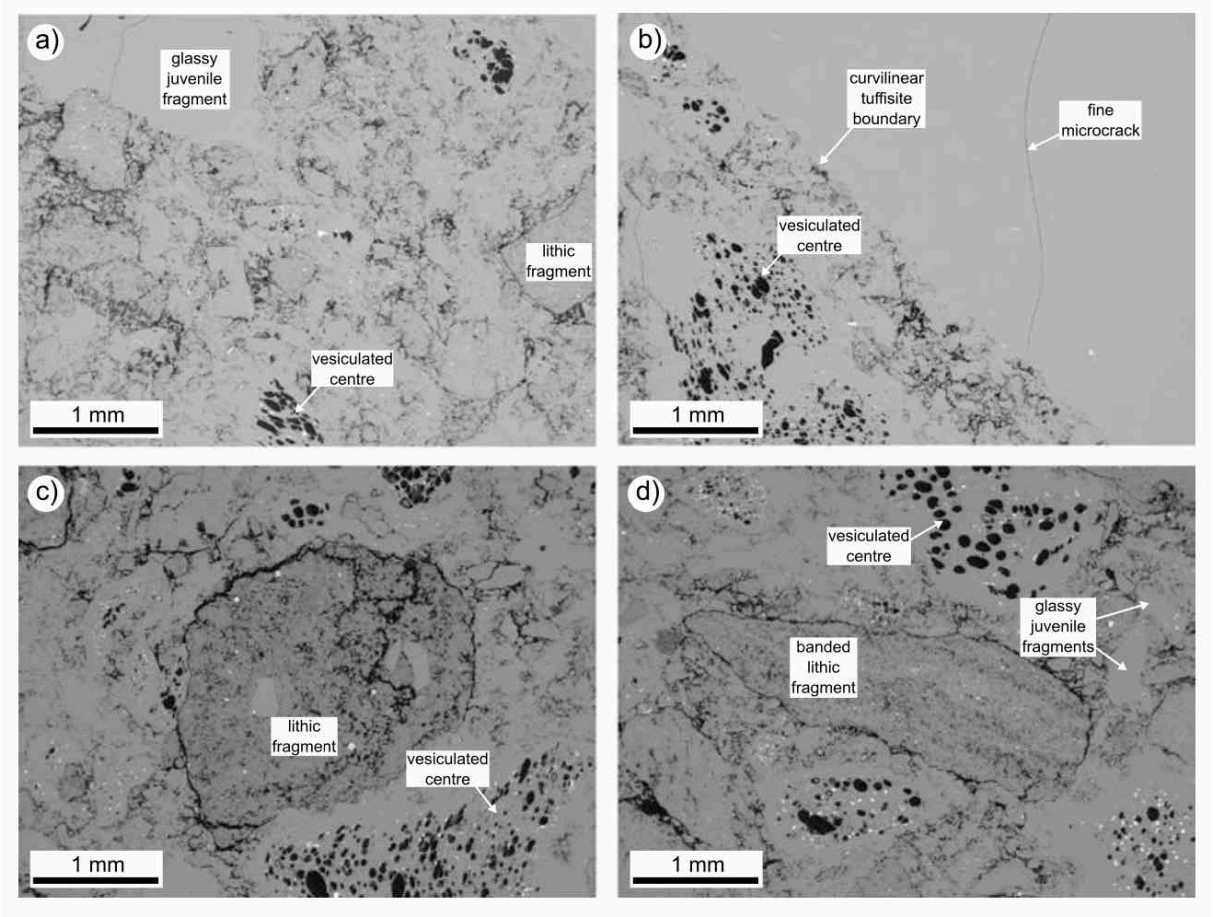

696

697 **Figure 3.** Backscattered scanning electron microscope (SEM) images of the BTB tuffisite. The
698 images show that the BTB tuffisite contains mixture of ash- and lapilli-sized juvenile and lithic
699 fragments. Some of the juvenile fragments have vesiculated centres (panels (a-d)). Lithic clasts
700 (rhyolite fragments) can be rounded (panel (c)) or banded/angular (panel (d)). Panel (b) shows
701 that the tuffisite-host rock boundary is curvilinear on the microscale.

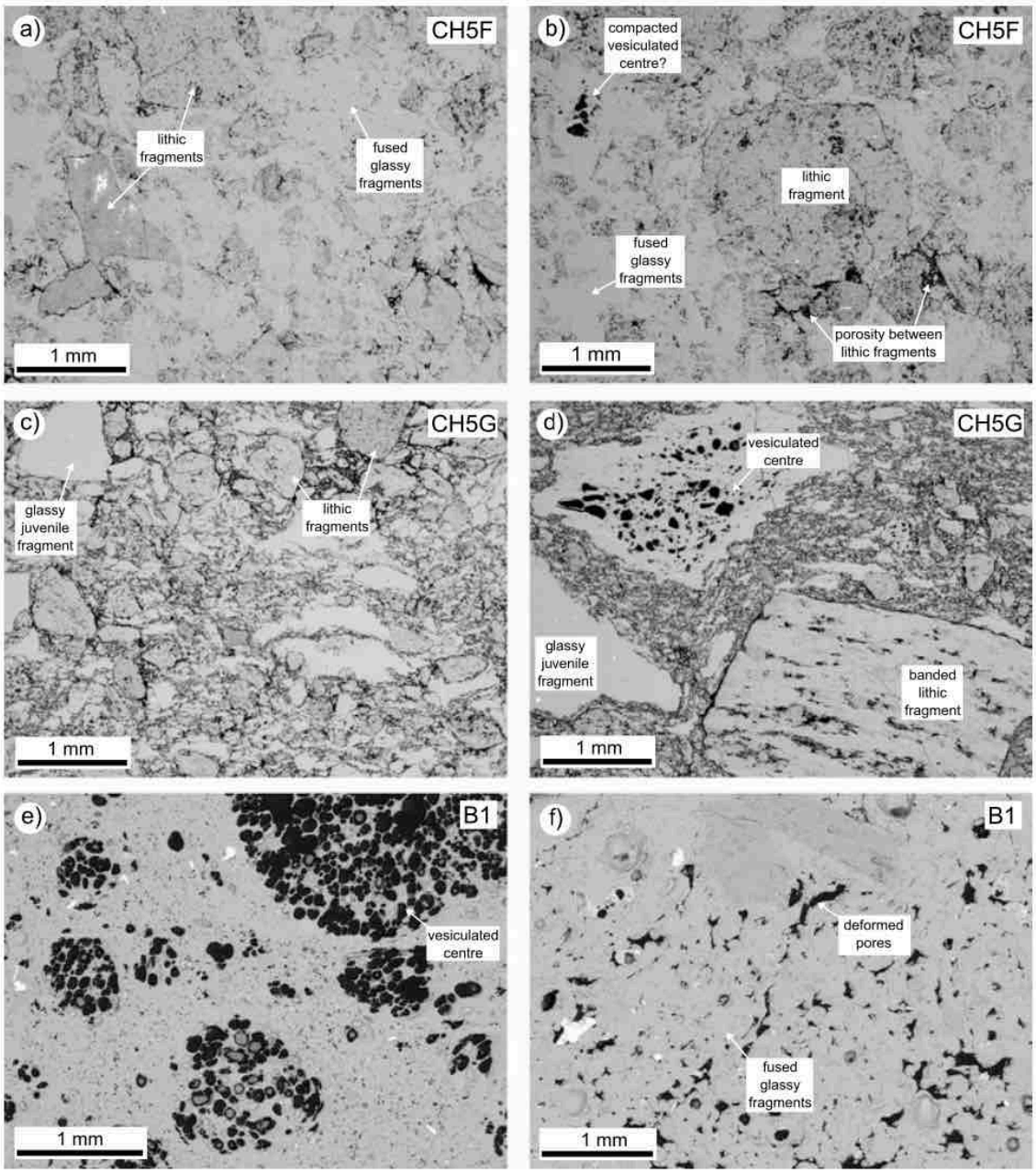

Figure 4. Backscattered scanning electron microscope (SEM) images of the CH5F (panels (a-b)), the CH5G (panels (c-d)), and the B1 (panels (e-f)) tuffisites. The images show that the tuffisites contain mixture of ash- and lapilli-sized juvenile and lithic fragments. Lithic clasts (rhyolite fragments) can be rounded (panels (b-c)) or banded/angular (panels (a) and (d)). Juvenile fragments with vesiculated centres can be seen in samples CH5G (panel (d)) and B1 (panel (e)), but are rare in sample CH5F (panel (b)). Glassy fragments are angular in sample CH5G (panels (c-d)), have diffuse boundaries in sample CH5F (panels (a-b)), and appear rounded in sample B1 (panel (f)).

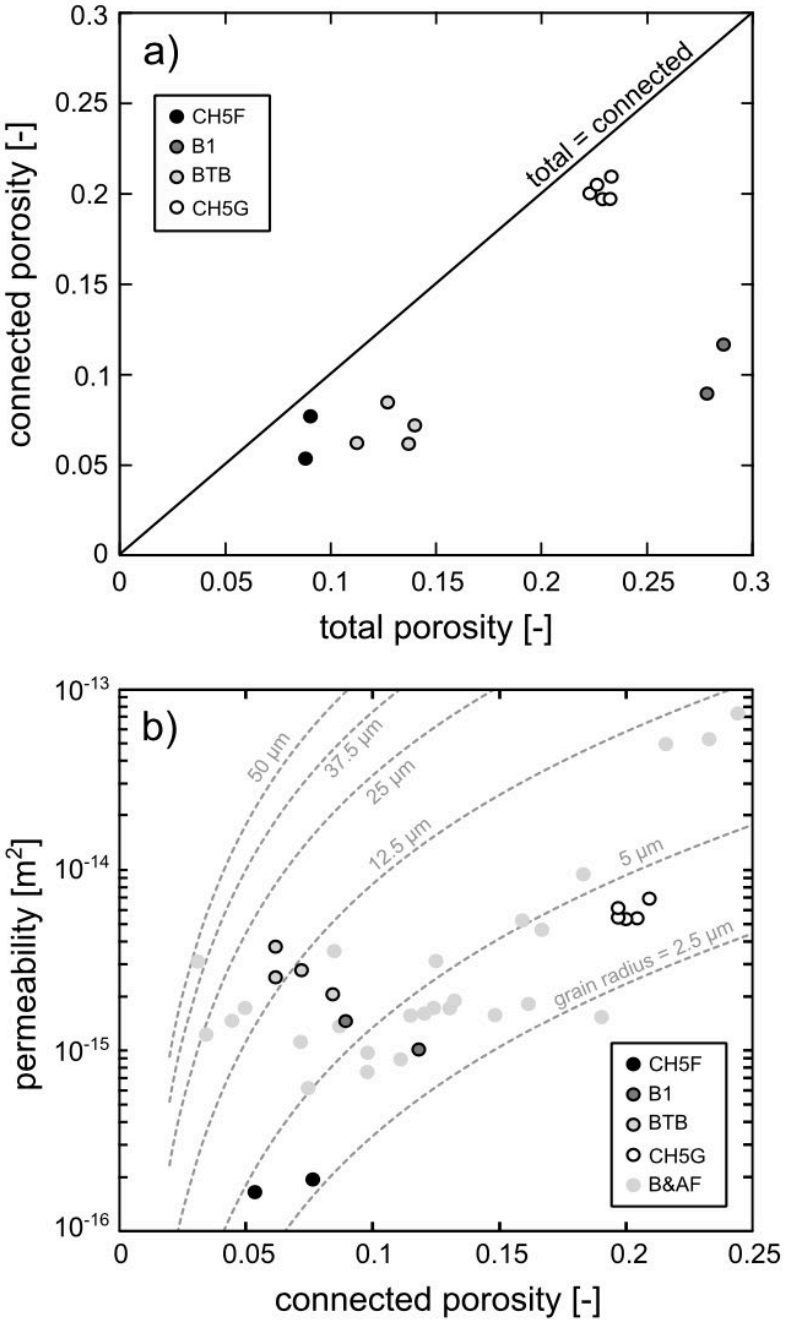

Figure 5. (a) Connected porosity as a function of total porosity for the four tuffisite samples (BTB, CH5F, CH5G, and B1). Measurement errors are smaller than the symbol size. (b) Permeability as a function of porosity for the four tuffisite samples (BTB, CH5F, CH5G, and B1). Measurement errors are smaller than the symbol size. Model curves (Equation 5) for a given initial particle radii are also provided as grey dashed lines (Wadsworth et al., 2016a) (see discussion for details). Data for variably sintered, granular volcanic material (welded block-and-ash flow; BAF) from Heap et al. (2015) are plotted to provide a comparison (light grey circles).

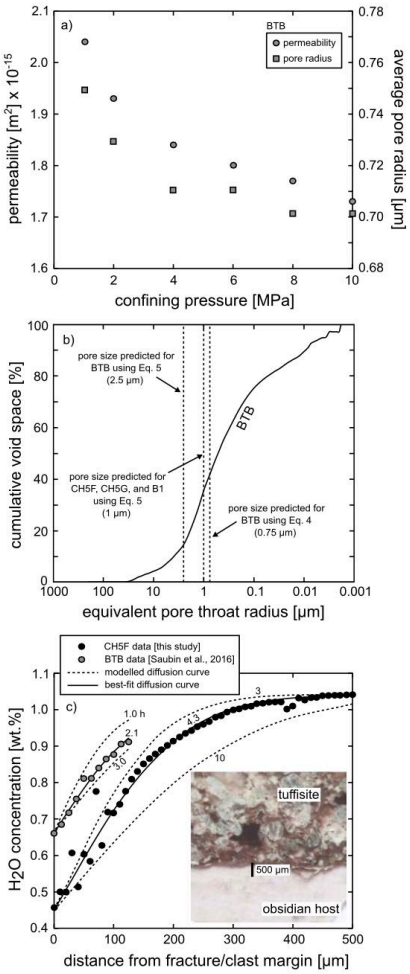

Figure 6. (a) Permeability as a function of confining pressure (up to 10 MPa) for a sample of BTB. Also shown is the average pore radius used by the gas molecules, as calculated using the Klinkenberg slip factor (Equation 4) (see discussion for details). (b) Pore throat size distribution (plot of cumulative void space as a function of pore throat diameter) determined using mercury porosimetry. The pore throat diameters determined using the Klinkenberg analysis (Equation (4)) and the permeability modelling (Equation (5)) are also indicated on the plot. (c) Measured spatial variation in H_2O from a clast margin for BTB (data from Saubin et al., 2016) and from the host rock obsidian for CH5F. Best-fit modelled 1D diffusion curves (solid lines) are given for each dataset (number in hours) (see discussion for details). We also provide neighbouring modelled 1D diffusion curves (dashed lines; number in hours) (see discussion for details). Inset on panel (c) shows a photograph showing the location of the profile in sample CH5F. Images of the transect for the BTB sample can be found in Saubin et al. (2016).

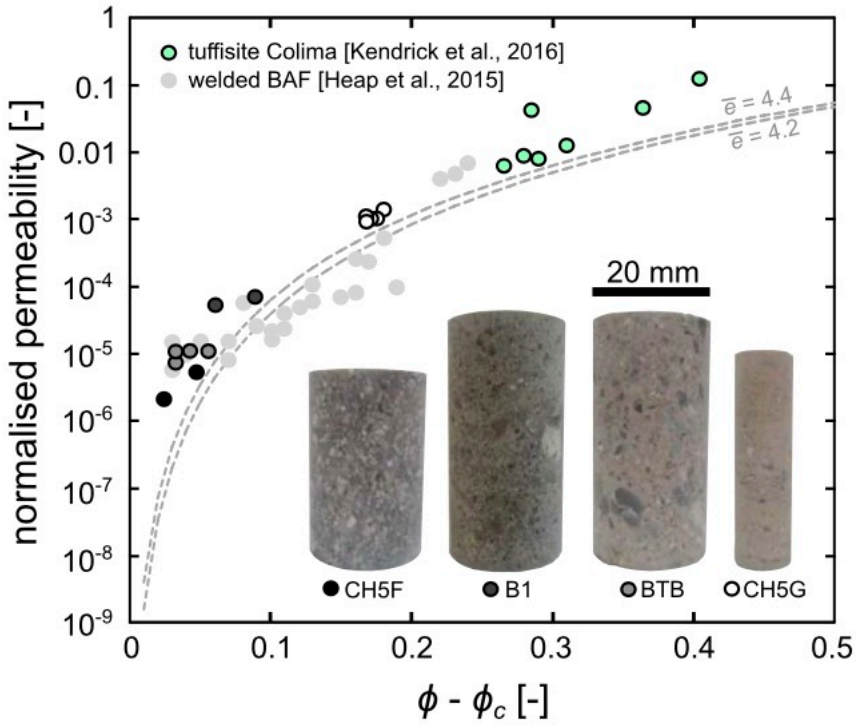

732

733 **Figure 7.** Normalised permeability (see text for details) as a function of $\phi - \phi_c$ (porosity minus
734 the porosity of the percolation threshold at which the permeability can be considered zero, taken
735 here as $\phi_c = 0.03$. The circles represent the experimental data (data unique to this study and data
736 from Heap et al. (2015) and Kendrick et al. (2016)) and collapse to a single permeability
737 description consistent with $4.2 < \bar{e} < 4.4$ (the two grey dashed curves) (see text for details).

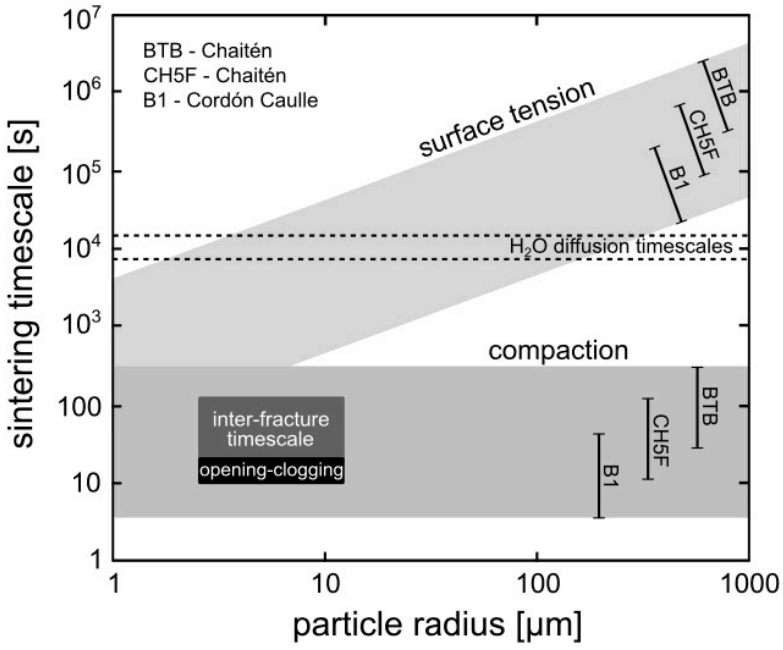

738

739 **Figure 8.** Sintering timescale as a function of particle radius for the two sintering regimes: surface
740 tension and compaction (grey zones). Timescales are provided for tuffisites from Chaitén
741 (samples BTB and CH5F) and Cordón Caulle (sample B1) using the range of viscosities determined
742 using a multicomponent viscosity model (Giordano et al., 2008) (see text for details). For the
743 range of particle radii thought to control sintering in the tuffisites of this study ($2.5 < \langle R \rangle < 15$
744 μm; estimated using a permeability model for granular materials; Wadsworth et al. (2016a); see
745 Figure 5), the sintering times for the surface tension regime are between 6 min and 5 h, between
746 16 min and 13.6 h, and between 2 min and 2.4 h for CH5F, BTB, and B1 respectively. Sintering
747 times in the compaction regime are predicted to be between 11 s and 2 min, between 28 s and 5
748 min, and between 3.5 s and 42 s for CH5F, BTB, and B1 respectively. We also plot the estimated
749 range for the time from fracture opening to clogging with pyroclastic debris, λ_1 (10-20 s, estimated
750 using video footage; Figure 1; Schipper et al., 2013) and the inter-fracture timescale ($\lambda_1 + \lambda$ or
751 $\lambda_1 + \lambda_2$) (20-120 s; Schipper et al., 2013). The calculated diffusion timescales for BTB and CH5F
752 (~2 and ~4 h, respectively) are indicated by the dashed lines. As these relate to diffusive H_2O
753 depletion in a ~millimetric clast (BTB) and the tuffisite wall (CH5F) they are independent of the
754 grainsize of the far finer-grained matrix (abscissa), and thus appear as horizontal lines.

Table 1. Summary of the porosity/permeability measurements performed for this study. Porosities quoted were measured at ambient laboratory pressure; the quoted confining pressure refers to the pressure used for the permeability measurements. Average pore radii were estimated using the Klinkenberg slip factor (see Equation 4 and text for details).

Sample	Total porosity	Connected porosity	Isolated porosity	Confining pressure (MPa)	Pore fluid	Permeability (m^2)	Correction	Klinkenberg slip factor (MPa)	Average pore radius (μm)
BTB-01	0.127	0.085	0.042	1	Argon	2.04×10^{-15}	Klinkenberg	0.0365	0.75
BTB-01	0.127	0.085	0.042	2	Argon	1.93×10^{-15}	Klinkenberg	0.0375	0.73
BTB-01	0.127	0.085	0.042	4	Argon	1.84×10^{-15}	Klinkenberg	0.0385	0.71
BTB-01	0.127	0.085	0.042	6	Argon	1.80×10^{-15}	Klinkenberg	0.0385	0.71
BTB-01	0.127	0.085	0.042	8	Argon	1.77×10^{-15}	Klinkenberg	0.0390	0.70
BTB-01	0.127	0.085	0.042	10	Argon	1.73×10^{-15}	Klinkenberg	0.0390	0.70
BTB-02	0.140	0.072	0.068	1	Nitrogen	2.77×10^{-15}	Forchheimer	-	-
BTB-03	0.113	0.062	0.051	1	Nitrogen	2.54×10^{-15}	Forchheimer	-	-
BTB-04	0.137	0.062	0.075	1	Nitrogen	3.73×10^{-15}	Forchheimer	-	-
BTB-07	0	0	0	1	Nitrogen	0	-	-	-
CH5_F-01	0.090	0.077	0.014	1	Nitrogen	1.91×10^{-16}	None	-	-
CH5_F-02	0.088	0.054	0.034	1	Nitrogen	1.63×10^{-16}	None	-	-
CH5_G-01	0.232	0.197	0.035	1	Nitrogen	6.12×10^{-15}	Forchheimer	-	-
CH5_G-02	0.223	0.200	0.023	1	Nitrogen	5.33×10^{-15}	Forchheimer	-	-
CH5_G-03	0.226	0.205	0.022	1	Nitrogen	5.37×10^{-15}	Forchheimer	-	-
CH5_G-04	0.233	0.209	0.023	1	Nitrogen	6.87×10^{-15}	Forchheimer	-	-
CH5_G-05	0.229	0.197	0.031	1	Nitrogen	5.40×10^{-15}	Forchheimer	-	-
B1	0.286	0.118	0.170	1	Nitrogen	1.03×10^{-15}	Forchheimer	-	-
B1	0.278	0.090	0.189	1	Nitrogen	1.48×10^{-15}	Forchheimer	-	-

References

Alloway, B. V., Pearce, N. J. G., Villarosa, G., Outes, V., & Moreno, P. I. (2015). Multiple melt bodies fed the AD 2011 eruption of Puyehue-Cordón Caulle, Chile. *Scientific Reports*, 5, 17589.

ASTM D4404-10, 2010. Standard Test Method for Determination of Pore Volume and Pore Volume Distribution of Soil and Rock by Mercury Intrusion Porosimetry. ASTM International, West Conshohocken, PA www.astm.org.

Behrens, H., & Nowak, M. (1997). The mechanisms of water diffusion in polymerized silicate melts. *Contributions to Mineralogy and Petrology*, *126*(4), 377-385. DOI: https://doi.org/10.1007/s004100050257.

Berlo, K., Tuffen, H., Smith, V. C., Castro, J. M., Pyle, D. M., Mather, T. A., & Geraki, K. (2013). Element variations in rhyolitic magma resulting from gas transport. *Geochimica et Cosmochimica Acta*, *121*, 436-451. DOI: https://doi.org/10.1016/j.gca.2013.07.032.

Black, B. A., Manga, M., & Andrews, B. (2016). Ash production and dispersal from sustained low-intensity Mono-Inyo eruptions. *Bulletin of Volcanology*, *78*(8), 57. DOI: https://doi.org/10.1007/s00445-016-1053-0.

Cabrera, A., Weinberg, R. F., Wright, H. M., Zlotnik, S., & Cas, R. A. (2011). Melt fracturing and healing: A mechanism for degassing and origin of silicic obsidian. *Geology*, *39*(1), 67-70. DOI: https://doi.org/10.1130/G31355.1.

Castro, J. M., & Dingwell, D. B. (2009). Rapid ascent of rhyolitic magma at Chaitén volcano, Chile. *Nature*, *461*(7265), 780. DOI: https://doi.org/10.1038/nature08458.

Castro, J. M., Cordonnier, B., Tuffen, H., Tobin, M. J., Puskar, L., Martin, M. C., & Bechtel, H. A. (2012). The role of melt-fracture degassing in defusing explosive rhyolite eruptions at volcán Chaitén. *Earth and Planetary Science Letters*, *333*, 63-69. DOI: https://doi.org/10.1016/j.epsl.2012.04.024.

Castro, J. M., Bindeman, I. N., Tuffen, H., & Schipper, C. I. (2014). Explosive origin of silicic lava: textural and δD–H2O evidence for pyroclastic degassing during rhyolite effusion. *Earth and Planetary Science Letters*, *405*, 52-61. DOI: https://doi.org/10.1016/j.epsl.2014.08.012.

Castro, J. M., Cordonnier, B., Schipper, C. I., Tuffen, H., Baumann, T. S., & Feisel, Y. (2016). Rapid laccolith intrusion driven by explosive volcanic eruption. *Nature Communications*, *7*, 13585. DOI: https://doi.org/10.1038/ncomms13585.

Chevalier, L., Collombet, M., & Pinel, V. (2017). Temporal evolution of magma flow and degassing conditions during dome growth, insights from 2D numerical modeling. *Journal of Volcanology and Geothermal Research*, 333, 116-133.

Civan, F. (2010). Effective correlation of apparent gas permeability in tight porous media. *Transport in Porous Media*, *82*(2), 375-384. DOI: https://doi.org/10.1007/s11242-009-9432-z.

Collinson, A. S. D., & Neuberg, J. W. (2012). Gas storage, transport and pressure changes in an evolving permeable volcanic edifice. *Journal of Volcanology and Geothermal Research*, *243*, 1-13. DOI: https://doi.org/10.1016/j.jvolgeores.2012.06.027.

Crank, J. (1979). *The Mathematics of Diffusion*. Oxford university press.

Diller, K., Clarke, A. B., Voight, B., & Neri, A. (2006). Mechanisms of conduit plug formation: Implications for vulcanian explosions. *Geophysical Research Letters*, 33(20).

Eichelberger, J. C., Carrigan, C. R., Westrich, H. R., & Price, R. H. (1986). Non-explosive silicic volcanism. *Nature*, *323*(6089), 598. DOI: https://doi.org/10.1038/323598a0.

Farquharson, J. I., Heap, M. J., Lavallée, Y., Varley, N. R., & Baud, P. (2016). Evidence for the development of permeability anisotropy in lava domes and volcanic conduits. *Journal of Volcanology and Geothermal Research*, *323*, 163-185. DOI: https://doi.org/10.1016/j.jvolgeores.2016.05.007.

Farquharson, J. I., Wadsworth, F. B., Heap, M. J., & Baud, P. (2017). Time-dependent permeability evolution in compacting volcanic fracture systems and implications for gas overpressure. *Journal of Volcanology and Geothermal Research*, *339*, 81-97. DOI: https://doi.org/10.1016/j.jvolgeores.2017.04.025.

Farquharson, J. I., & Wadsworth, F. B. (2018). Upscaling permeability in anisotropic volcanic systems. *Journal of Volcanology and Geothermal Research*, 364, 35-47.

Feng, S., Halperin, B. I., & Sen, P. N. (1987). Transport properties of continuum systems near the percolation threshold. *Physical Review B*, *35*(1), 197. DOI: https://doi.org/10.1103/PhysRevB.35.197.

Firouzi, M., Alnoaimi, K., Kovscek, A., & Wilcox, J. (2014). Klinkenberg effect on predicting and measuring helium permeability in gas shales. *International Journal of Coal Geology*, *123*, 62-68. DOI: https://doi.org/10.1016/j.coal.2013.09.006.

Forchheimer, P. (1901). Wasserbewegung durch boden. *Z. Ver. Deutsch, Ing.*, *45*, 1782-1788.

Fowler, A. C., & Scheu, B. (2016). A theoretical explanation of grain size distributions in explosive rock fragmentation. *Proc. R. Soc. A*, *472*(2190), 20150843. DOI: https://doi.org/10.1098/rspa.2015.0843.

Gardner, J. E., & Ketcham, R. A. (2011). Bubble nucleation in rhyolite and dacite melts: temperature dependence of surface tension. *Contributions to Mineralogy and Petrology*, *162*(5), 929-943. DOI: https://doi.org/10.1007/s00410-011-0632-5.

Gardner, J. E., Llewellin, E. W., Watkins, J. M., & Befus, K. S. (2017). Formation of obsidian pyroclasts by sintering of ash particles in the volcanic conduit. *Earth and Planetary Science Letters*, *459*, 252-263. DOI: https://doi.org/10.1016/j.epsl.2016.11.037.

Gardner, J. E., Wadsworth, F. B., Llewellin, E. W., Watkins, J. M., & Coumans, J. P. (2018). Experimental sintering of ash at conduit conditions and implications for the longevity of tuffisites. *Bulletin of Volcanology*, *80*(3), 23. DOI: https://doi.org/10.1007/s00445-018-1202-8.

Giordano, D., Russell, J. K., & Dingwell, D. B. (2008). Viscosity of magmatic liquids: a model. *Earth and Planetary Science Letters*, *271*(1-4), 123-134. DOI: https://doi.org/10.1016/j.epsl.2008.03.038.

Gonnermann, H. M., & Manga, M. (2003). Explosive volcanism may not be an inevitable consequence of magma fragmentation. *Nature*, *426*(6965), 432. DOI: https://doi.org/10.1038/nature02138.

Heap, M. J., Kolzenburg, S., Russell, J. K., Campbell, M. E., Welles, J., Farquharson, J. I., & Ryan, A. (2014). Conditions and timescales for welding block-and-ash flow deposits. *Journal of Volcanology and Geothermal Research*, *289*, 202-209. DOI: https://doi.org/10.1016/j.jvolgeores.2014.11.010.

Heap, M. J., Farquharson, J. I., Wadsworth, F. B., Kolzenburg, S., & Russell, J. K. (2015). Timescales for permeability reduction and strength recovery in densifying magma. *Earth and Planetary Science Letters*, *429*, 223-233. DOI: https://doi.org/10.1016/j.epsl.2015.07.053.

Heap, M. J., & Kennedy, B. M. (2016). Exploring the scale-dependent permeability of fractured andesite. *Earth and Planetary Science Letters*, *447*, 139-150. DOI: https://doi.org/10.1016/j.epsl.2016.05.004.

Heap, M. J., Kushnir, A. R., Gilg, H. A., Wadsworth, F. B., Reuschlé, T., & Baud, P. (2017). Microstructural and petrophysical properties of the Permo-Triassic sandstones (Buntsandstein) from the Soultz-sous-Forêts geothermal site (France). *Geothermal Energy*, *5*(1), 26. DOI: https://doi.org/10.1186/s40517-017-0085-9.

Heap, M. J., Reuschlé, T., Farquharson, J. I., & Baud, P. (2018a). Permeability of volcanic rocks to gas and water. *Journal of Volcanology and Geothermal Research*, *354*, 29-38. DOI: https://doi.org/10.1016/j.jvolgeores.2018.02.002.

Heap, M., Reuschlé, T., Baud, P., Renard, F., & Iezzi, G. (2018b). The permeability of stylolite-bearing limestone. *Journal of Structural Geology*, *116*, 81-93. DOI: https://doi.org/10.1016/j.jsg.2018.08.007.

Heap, M. J. (2019). The influence of sample geometry on the permeability of a porous sandstone. *Geoscientific Instrumentation, Methods and Data Systems*, 8(1), 55-61.

Heiken, G., Wohletz, K., & Eichelberger, J. (1988). Fracture fillings and intrusive pyroclasts, Inyo Domes, California. *Journal of Geophysical Research: Solid Earth*, *93*(B5), 4335-4350. DOI: https://doi.org/10.1029/JB093iB05p04335.

Heller, R., Vermylen, J., & Zoback, M. (2014). Experimental investigation of matrix permeability of gas shales. *AAPG Bulletin*, *98*(5), 975-995. DOI: https://doi.org/10.1306/09231313023.

Holland, A. P., Watson, I. M., Phillips, J. C., Caricchi, L., & Dalton, M. P. (2011). Degassing processes during lava dome growth: Insights from Santiaguito lava dome, Guatemala. *Journal of Volcanology and Geothermal Research*, *202*(1-2), 153-166. DOI: https://doi.org/10.1016/j.jvolgeores.2011.02.004.

Ihinger, P. D., Hervig, R. L., & McMillan, P. F. (1994). Analytical methods for volatiles in glasses. *Reviews in Mineralogy and Geochemistry*, *30*(1), 67-121.

Johnson, J. B., Lees, J. M., Gerst, A., Sahagian, D., & Varley, N. (2008). Long-period earthquakes and co-eruptive dome inflation seen with particle image velocimetry. *Nature*, *456*(7220), 377. DOI: https://doi.org/10.1038/nature07429.

Kemmer, G., & Keller, S. (2010). Nonlinear least-squares data fitting in Excel spreadsheets. *Nature Protocols*, *5*(2), 267. DOI: https://doi.org/10.1038/nprot.2009.182.

Kendrick, J. E., Lavallée, Y., Varley, N. R., Wadsworth, F. B., Lamb, O. D., & Vasseur, J. (2016). Blowing off steam: tuffisite formation as a regulator for lava dome eruptions. *Frontiers in Earth Science*, *4*, 41. DOI: https://doi.org/10.3389/feart.2016.00041.

Kennedy, B. M., Wadsworth, F. B., Vasseur, J., Schipper, C. I., Jellinek, A. M., von Aulock, F. W., et al. (2016). Surface tension driven processes densify and retain permeability in magma and lava. *Earth and Planetary Science Letters*, *433*, 116-124. DOI: https://doi.org/10.1016/j.epsl.2015.10.031.

876 Klinkenberg, L. J. (1941). The permeability of porous media to liquids and gases. In *Drilling and production*
877 *practice*. American Petroleum Institute.
878 Kolzenburg, S., Heap, M., Lavallée, Y., Russell, J., Meredith, P., & Dingwell, D. B. (2012). Strength and
879 permeability recovery of tuffisite-bearing andesite. *Solid Earth*, *3*, 191-198. DOI:
880 https://doi.org/10.5194/se-3-191-2012.
881 Kolzenburg, S., & Russell, J. K. (2014). Welding of pyroclastic conduit infill: A mechanism for cyclical
882 explosive eruptions. *Journal of Geophysical Research: Solid Earth*, *119*(7), 5305-5323. DOI:
883 https://doi.org/10.1002/2013JB010931.
884 Kueppers, U., Scheu, B., Spieler, O., & Dingwell, D. B. (2006). Fragmentation efficiency of explosive volcanic
885 eruptions: a study of experimentally generated pyroclasts. *Journal of Volcanology and Geothermal*
886 *Research*, *153*(1-2), 125-135. DOI: https://doi.org/10.1016/j.jvolgeores.2005.08.006.
887 Kushnir, A. R., Martel, C., Champallier, R., & Arbaret, L. (2017). In situ confirmation of permeability
888 development in shearing bubble-bearing melts and implications for volcanic outgassing. *Earth and*
889 *Planetary Science Letters*, *458*, 315-326. DOI: https://doi.org/10.1016/j.epsl.2016.10.053.
890 Letham, E. A., & Bustin, R. M. (2016). Klinkenberg gas slippage measurements as a means for shale pore
891 structure characterization. *Geofluids*, *16*(2), 264-278. DOI: https://doi.org/10.1111/gfl.12147.
892 Lara, L. E. (2010). The 2008 eruption of the Chaitén Volcano, Chile: a preliminary report. *Andean*
893 *Geology*, *36*(1), 125-130. DOI: http://dx.doi.org/10.5027/andgeoV36n1-a09.
894 Martys, N. S., Torquato, S., & Bentz, D. P. (1994). Universal scaling of fluid permeability for sphere
895 packings. *Physical Review E*, *50*(1), 403. DOI: https://doi.org/10.1103/PhysRevE.50.403.
896 McKenzie, D. (2011). Compaction and crystallization in magma chambers: Towards a model of the
897 Skaergaard intrusion. *Journal of Petrology*, *52*(5), 905-930. DOI:
898 https://doi.org/10.1093/petrology/egr009.
899 Militzer, A. S. (2013). The P-T-x evolution of the 2011-12 explosively and effusively erupted rhyolites at
900 Puyehue-Cordón Caulle, Chile. Diplomarbeit, Univ. Mainz, 93 pp.
901 Nara, Y., Meredith, P. G., Yoneda, T., & Kaneko, K. (2011). Influence of macro-fractures and micro-fractures
902 on permeability and elastic wave velocities in basalt at elevated pressure. *Tectonophysics*, *503*(1-
903 2), 52-59. DOI: https://doi.org/10.1016/j.tecto.2010.09.027.
904 Neuberg, J. W., Tuffen, H., Collier, L., Green, D., Powell, T., & Dingwell, D. (2006). The trigger mechanism of
905 low-frequency earthquakes on Montserrat. *Journal of Volcanology and Geothermal Research*, *153*(1-
906 2), 37-50. DOI: https://doi.org/10.1016/j.jvolgeores.2005.08.008.
907 Newman, S., Stolper, E. M., & Epstein, S. (1986). Measurement of water in rhyolitic glasses; calibration of an
908 infrared spectroscopic technique. *American Mineralogist*, *71*(11-12), 1527-1541.
909 Okumura, S., Nakamura, M., & Nakashima, S. (2003). Determination of molar absorptivity of IR fundamental
910 OH-stretching vibration in rhyolitic glasses. *American Mineralogist*, *88*(11-12), 1657-1662. DOI:
911 https://doi.org/10.2138/am-2003-11-1204.
912 Okumura, S., & Sasaki, O. (2014). Permeability reduction of fractured rhyolite in volcanic conduits and its
913 control on eruption cyclicity. *Geology*, *42*(10), 843-846. DOI: https://doi.org/10.1130/G35855.1.
914 Owen, J., Shea, T., & Tuffen, H. (2019). Basalt, unveiling fluid-filled fractures, inducing sediment intra-void
915 transport, ephemerally: Examples from Katla 1918. *Journal of Volcanology and Geothermal*
916 *Research*. DOI: https://doi.org/10.1016/j.jvolgeores.2018.11.002.
917 Pallister, J. S., Diefenbach, A. K., Burton, W. C., Muñoz, J., Griswold, J. P., Lara, L. E., et al. (2013). The Chaitén
918 rhyolite lava dome: Eruption sequence, lava dome volumes, rapid effusion rates and source of the
919 rhyolite magma. *Andean Geology*, *40*(2), 277-294. DOI: http://dx.doi.org/10.5027/andgeoV40n2-
920 a06.
921 Quane, S. L., Russell, J. K., & Friedlander, E. A. (2009). Time scales of compaction in volcanic
922 systems. *Geology*, *37*(5), 471-474. DOI: https://doi.org/10.1130/G25625A.1.
923 Rintoul, M. D. (2000). Precise determination of the void percolation threshold for two distributions of
924 overlapping spheres. *Physical Review E*, *62*(1), 68. DOI: https://doi.org/10.1103/PhysRevE.62.68.
925 Russell, J. K., & Quane, S. L. (2005). Rheology of welding: inversion of field constraints. *Journal of Volcanology*
926 *and Geothermal Research*, *142*(1-2), 173-191. DOI:
927 https://doi.org/10.1016/j.jvolgeores.2004.10.017.
928 Rust, A. C., Cashman, K. V., & Wallace, P. J. (2004). Magma degassing buffered by vapor flow through
929 brecciated conduit margins. *Geology*, *32*(4), 349-352. DOI: https://doi.org/10.1130/G20388.2.
930 Ryan, A. G., Friedlander, E. A., Russell, J. K., Heap, M. J., & Kennedy, L. A. (2018a). Hot pressing in conduit
931 faults during lava dome extrusion: Insights from Mount St. Helens 2004–2008. *Earth and Planetary*
932 *Science Letters*, *482*, 171-180. DOI: https://doi.org/10.1016/j.epsl.2017.11.010.
933 Ryan, A.G., Russell, J.K., and Heap, M.J. (2018b). Rapid solid-state sintering in volcanic systems. *American*
934 *Mineralogist*. DOI: https://doi.org/10.2138/am-2018-6714.

935 Ryan, A.G., Russell, J.K., Heap, M.J., Kolzenburg, S., Vona, A., and Kushnir, A.R.L. (2019). Strain-dependent
936 rheology of silicate melt foams: importance for outgassing of silicic lavas. *Journal of Geophysical*
937 *Research: Solid Earth*, accepted.
938 Saubin, E., Tuffen, H., Gurioli, L., Owen, J., Castro, J. M., Berlo, K., et al. (2016). Conduit dynamics in transitional
939 rhyolitic activity recorded by tuffisite vein textures from the 2008–2009 Chaitén
940 Eruption. *Frontiers in Earth Science*, *4*, 59. DOI: https://doi.org/10.3389/feart.2016.00059.
941 Schipper, C. I., Castro, J. M., Tuffen, H., James, M. R., & How, P. (2013). Shallow vent architecture during hybrid
942 explosive–effusive activity at Cordón Caulle (Chile, 2011–12): evidence from direct observations
943 and pyroclast textures. *Journal of Volcanology and Geothermal Research*, *262*, 25-37. DOI:
944 https://doi.org/10.1016/j.jvolgeores.2013.06.005.
945 Stasiuk, M. V., Barclay, J., Carroll, M. R., Jaupart, C., Ratté, J. C., Sparks, R. S. J., & Tait, S. R. (1996). Degassing
946 during magma ascent in the Mule Creek vent (USA). *Bulletin of Volcanology*, *58*(2-3), 117-130. DOI:
947 https://doi.org/10.1007/s004450050130.
948 Stix, J., Zapata G, J. A., Calvache V, M., Cortés J, G. P., Fischer, T. P., Gómez M, D., ... & Williams, S. N. (1993). A
949 model of degassing at Galeras Volcano, Colombia, 1988-1993. *Geology*, 21(11), 963-967.
950 Torquato, S. (2013). *Random Heterogeneous Materials: Microstructure and Macroscopic Properties* (Vol. 16).
951 Springer Science & Business Media.
952 Torquato, S., & Avellaneda, M. (1991). Diffusion and reaction in heterogeneous media: Pore size distribution,
953 relaxation times, and mean survival time. *The Journal of Chemical Physics*, *95*(9), 6477-6489. DOI:
954 https://doi.org/10.1063/1.461519.
955 Tuffen, H., Dingwell, D. B., & Pinkerton, H. (2003). Repeated fracture and healing of silicic magma generate
956 flow banding and earthquakes? *Geology*, *31*(12), 1089-1092. DOI:
957 https://doi.org/10.1130/G19777.1.
958 Tuffen, H., & Dingwell, D. (2005). Fault textures in volcanic conduits: evidence for seismic trigger
959 mechanisms during silicic eruptions. *Bulletin of Volcanology*, *67*(4), 370-387. DOI:
960 https://doi.org/10.1007/s00445-004-0383-5.
961 Vasseur, J., Wadsworth, F. B., Lavallée, Y., Hess, K. U., & Dingwell, D. B. (2013). Volcanic sintering: timescales
962 of viscous densification and strength recovery. *Geophysical Research Letters*, *40*(21), 5658-5664.
963 DOI: https://doi.org/10.1002/2013GL058105.
964 Voight, B., Sparks, R. S. J., Miller, A. D., Stewart, R. C., Hoblitt, R. P., Clarke, A., et al. (1999). Magma flow
965 instability and cyclic activity at Soufriere Hills volcano, Montserrat, British West Indies.
966 *Science*, *283*(5405), 1138-1142. DOI: https://doi.org/10.1126/science.283.5405.1138.
967 von Aulock, F. W., Kennedy, B. M., Schipper, C. I., Castro, J. M., Martin, D. E., Oze, C., et al. (2014). Advances in
968 Fourier transform infrared spectroscopy of natural glasses: From sample preparation to data
969 analysis. *Lithos*, *206*, 52-64. DOI: https://doi.org/10.1016/j.lithos.2014.07.017.
970 Wadsworth, F. B., Vasseur, J., von Aulock, F. W., Hess, K. U., Scheu, B., Lavallée, Y., & Dingwell, D. B. (2014).
971 Nonisothermal viscous sintering of volcanic ash. *Journal of Geophysical Research: Solid*
972 *Earth*, *119*(12), 8792-8804. DOI: https://doi.org/10.1002/2014JB011453.
973 Wadsworth, F. B., Vasseur, J., Scheu, B., Kendrick, J. E., Lavallée, Y., & Dingwell, D. B. (2016a). Universal
974 scaling of fluid permeability during volcanic welding and sediment diagenesis. *Geology*, *44*(3), 219-
975 222. DOI: https://doi.org/10.1130/G37559.1.
976 Wadsworth, F. B., Vasseur, J., Llewellin, E. W., Schauroth, J., Dobson, K. J., Scheu, B., & Dingwell, D. B. (2016b).
977 Sintering of viscous droplets under surface tension. *Proc. R. Soc. A*, *472*(2188), 20150780. DOI:
978 https://doi.org/10.1098/rspa.2015.0780.
979 Wadsworth, F. B., Vasseur, J., Llewellin, E. W., & Dingwell, D. B. (2017a). Sintering of polydisperse viscous
980 droplets. *Physical Review E*, *95*(3), 033114. DOI: https://doi.org/10.1103/PhysRevE.95.033114.
981 Wadsworth, F. B., Vasseur, J., Llewellin, E. W., Dobson, K. J., Colombier, M., von Aulock, F. W., et al. (2017b).
982 Topological inversions in coalescing granular media control fluid-flow regimes. *Physical Review*
983 *E*, *96*(3), 033113. DOI: https://doi.org/10.1103/PhysRevE.96.033113.
984 Watkins, J. M., Gardner, J. E., & Befus, K. S. (2017). Nonequilibrium degassing, regassing, and vapor fluxing
985 in magmatic feeder systems. *Geology*, *45*(2), 183-186. DOI: https://doi.org/10.1130/G38501.1.
986 Zhang, Y. (1999). H2O in rhyolitic glasses and melts: measurement, speciation, solubility, and
987 diffusion. *Reviews of Geophysics*, *37*(4), 493-516. DOI: https://doi.org/10.1029/1999RG900012.